TRAC method in dissipative media -Part I: Analysis in 1D and frequency domain

Marie Graff, Mina Cullen

TRAC method in dissipative media – Part I: Analysis in 1D and frequency domain

Marie Graff and Mina Cullen
Department of Mathematics, University of Auckland, Auckland, New Zealand
Corresponding author: marie.graff@auckland.ac.nz

February 28, 2022

Abstract

In this paper, we propose to explore the Time-Reversed Absorbing Condition (*TRAC*) method in the case of dissipative homogeneous media. In previous work, the *TRAC* method was derived from the time-reversibility of the (undamped) wave equation and proved to be efficient in both the time-domain and the frequency-domain. Namely, two main utilisations of the *TRAC* method have been probed: (a) *redatuming*, i.e., moving virtually the measurements by reconstructing the wavefield and (b) tracking down the location of a possible inclusion inside the domain.

However, many applications working with waves, and in need of redatuming for instance, require to add a dissipative component to their model. Accordingly, a study of the *TRAC* method in the case of dissipation is relevant and, in particular, we will see that performing the standard *TRAC* method, i.e., ignoring the dissipation, does not give satisfactory results.

An analysis is provided in the frequency-domain and one-space dimension and shows satisfactory updated versions of the *TRAC* method. Numerical examples in 1D and 2D are presented to illustrate the results.

1 Introduction, principle and motivation

It has been about thirty years since Time Reversal (TR) was introduced by Matthias Fink as a response to imaging problems [1, 2]. The principle of TR is to take advantage of the time reversibility of the undamped wave equation to reconstruct the wavefield from measurements recorded on a receivers' array, also called Time Reversal Mirror (TRM) [3, 4]. These data are time-reversed and sent back into the domain, creating a wavefield propagating back, and through, any heterogeneous components included in the domain. This has been widely advertised as "recreating the past" in the TR community.

Many work on TR has been done since the seminal papers. In particular, even though Time Reversal is a powerful tool and is robust even with respect to complex media, the generated time-reversed wavefield back-propagating in the ambient medium to its original source has a non-decreasing energy due to the diffraction limit [1, 5]. Therefore, a focal spot is observed at the location of the source, which prevents a good resolution of the image. In [6, 7], the authors proposed a way to limit the effects of the diffraction limit while working with Time Reversal Mirrors. To tackle this issue, a study about the Time Reversal Operator Decomposition was also achieved to gain a better understanding of the technique [8, 9]. Other techniques using

filtering also examined ways to reduce the diffraction limit and improve the resolution of the image [10, 11, 12] in the context of heterogeneous media, summarised in 2013 in [13]. Some theoretical results were also proposed for dissipative media in [14, 15].

About ten years ago, an alternative was proposed in order to remove the issue of the diffraction limit, via a numerical method called *TRAC* for Time Reversed Absorbing Condition [16, 17, 18]. The main idea of this method is to introduce an artificial sink, also called trial domain, in the computational domain that encloses the source or the scatterer acting as a passive source. The choice of the boundary condition to impose on the new artificial boundary is crucial and it has been proven that a time-reversed absorbing boundary condition was the right condition [16], hence the name of the method. Then, the type and order of the chosen absorbing boundary condition (ABC) totally depends on the shape of the artificial boundary and the level of accuracy one wants to reach.

There has been many work on absorbing or non-reflecting boundary conditions, since the first papers [19, 20, 21], namely for different shapes like in [22, 23, 24] for an ellipse and [25, 26] for arbitrary shapes. A wide literature also consider the question of the accuracy by developing always higher-order of approximation of the ABC, see for instance [27, 28, 29, 30, 31, 32]. Moreover, the ABC actually depends on the model as well. Therefore, many types of ABCs have been designed for the acoustic waves in the case of heterogeneous media [29, 33] and multiple scattering [34, 35, 36]. Then, for the Maxwell equations, non-reflecting boundary conditions are proposed in [37, 38, 39], and for the elastic waves see [40, 41, 42, 43].

The *TRAC* method has two main applications. The first application is the ability to reduce the size of the computational domain by moving virtually the measured data from the receivers' array to the artificial trial domain. This principle is known as *redatuming* and was first developed for seismic waves [44] and later generalised in [45]. This first application has been explored for the *TRAC* method in [46, 47] and coupled with inverse problem techniques to corroborate the fact that the new gathered virtual data provide a good reconstruction of the expected image in a considerably reduced computational domain. This naturally improved the cost in terms of computational time and storage for the subsequent inverse problem. More recently, full waveform redatuming has been explored via a least-squares version of the *TRAC* method in [48].

The second application of the *TRAC* method consists of tracking inclusions or scatterers. The method is using the information provided via the reconstruction of the wavefield to determine the location of the scatterer. It has been indeed shown that a bad position of the trial domain, i.e., not enclosing entirely the scatterer, would lead to an erroneous reconstruction of the wavefield. By considering the associated error, the position of the trial domain can be corrected to locate the inclusion better. This has been studied in [17, 18, 49], but also for crack and source identification in [50, 51, 52]. Recently, an algorithm for an automatic detection of the inclusion has been proposed in [53].

The novelty of this paper is to consider a dissipative version of the *TRAC* method. Until now, the computational domain was always assumed homogeneous, constant and non-dissipative, which limited its utilisation in real applications containing dissipation. Therefore, we propose a study of the method when an anti-dissipative term is added by time reversal. We will derive simple absorbing boundary conditions including the dissipative component, since it seems that very little work has been proposed on that topic. Only recently, Barucq *et al.* [54] designed absorbing boundary conditions in the context of 3D atmospheric waves, whose model contains a damping term. Our 1D and 2D results are consistent with the ABCs derived in [54]. A Part II on heterogeneous media is planned to complete this study.

A reminder of the principle of the *TRAC* method in the frequency domain, followed by research questions studied through this paper, complete this introductory section.

In the rest of the paper, we consider the wave equation in the frequency domain[1], which will be explicitly expressed using the Helmholtz equation. By doing so, we are able to compute by hand (or using symbolic calculators such as Maple) solutions to the forward problem and diverse versions of the time reversed counterparts of the forward problem.

1.1 Principle of the *TRAC* method: a reminder in the frequency domain

We consider an inclusion D living in some known medium, which can be assumed homogeneous or not, dissipative or not. A source f generates an incident wavefield u^I that impinges on the inclusion, whose scattering response is recorded on a receivers' array. The resulting forward total wavefield u^T satisfies:

$$-\omega^2\kappa u^T - \Delta u^T \;=\; f, \qquad \text{in } \mathbb{R}^d, \tag{1}$$

with Sommerfeld radiation conditions. In (1), ω denotes the frequency, d is the dimension, likely to be 1, 2 or 3. Parameter κ represents the physical properties of the medium and the inclusion, and can be defined as:

$$\kappa(\vec{x}) \;:=\; \frac{1}{c^2(\vec{x})}\left(1 - i\frac{\sigma(\vec{x})}{\omega}\right), \tag{2}$$

where c is the wave propagation speed, σ the dissipation and $i = \sqrt{-1}$. Both c and σ are assumed to be functions in space with possible discontinuity at the interface between the inclusion and the surrounding medium. As such, we use the following notation: the subscript 0 is used for the surrounding medium while the subscript D is for the inclusion. The characteristic function χ_D defines the area delimited by the boundary of the inclusion D. Thus,

$$c(\vec{x}) := c_0(\vec{x}) + (c_D(\vec{x}) - c_0(\vec{x}))\chi_D(\vec{x}), \quad \text{and} \quad \sigma(\vec{x}) := \sigma_0(\vec{x}) + (\sigma_D(\vec{x}) - \sigma_0(\vec{x}))\chi_D(\vec{x}).$$

Remark 1.1. For some applications using electromagnetic waves, the Helmholtz equation is used as a good approximation [56, 57, 58]. In this case, the parameters involved are the electric permittivity ε, the magnetic permeability μ and the electric conductivity σ, the latter inducing damping. With these notations, κ becomes:

$$\kappa(\vec{x}) \;:=\; \mu(\vec{x})\left(\varepsilon(\vec{x}) - i\sigma(\vec{x})/\omega\right). \qquad \blacksquare$$

Our aim is to reconstruct the total wavefield from measurements using time reversal techniques [1, 2]. To do so, we introduce a bounded computational domain Ω. We also denote by Γ the receivers' array, which may be part or not of $\partial\Omega$, and which may be continuous or discrete, see Figure 1. To perform the *TRAC* method, we also introduce an artificial domain B, usually a ball, which is assumed to enclose inclusion D. As already developed in previous papers [17, 18], the time-reversed total wavefield v_R^T can be reconstructed when solving:

$$\left\{\begin{array}{rcll} -\omega^2\overline{\kappa}v_R^T - \Delta v_R^T & = & 0, & \text{in } \Omega\backslash B, \\ v_R^T & = & \overline{u^T}, & \text{on } \Gamma, \\ \text{TRAC}(v_R^T) & = & \text{TRAC}(\overline{u^I}), & \text{on } \partial B, \end{array}\right. \tag{3}$$

with appropriate radiation conditions on the boundary $\partial\Omega$, if relevant. Note that time reversal in the frequency domain corresponds to complex conjugation [17], which is denoted by an overline here.

[1] using the following convention: the Fourier transform of the time derivative becomes $i\omega$, see [55].

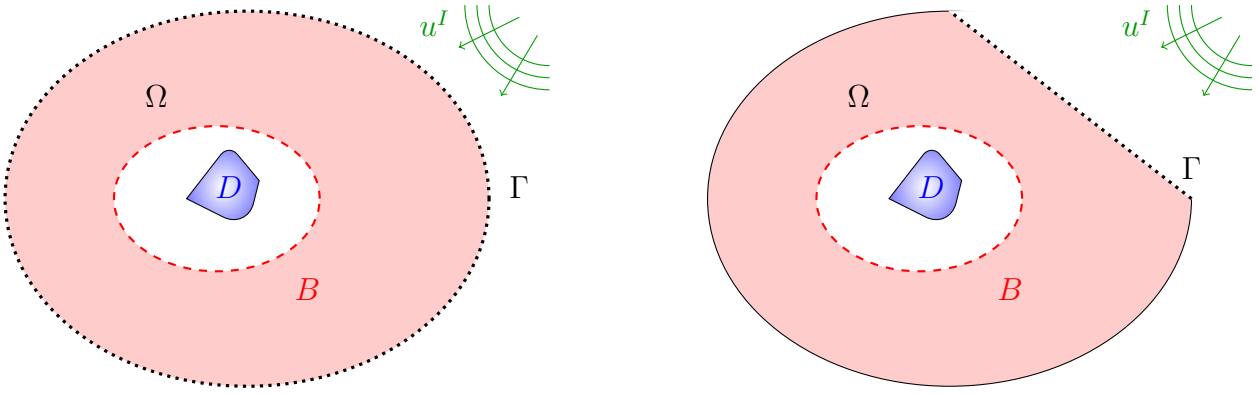

(a) Full aperture (b) Partial aperture

Figure 1: Geometry of the domain: trial domain B encloses perfectly inclusion D. The receivers' array Γ may be on the entire boundary of Ω or only partially.

Claim 1.1. *If the chosen time reversed absorbing boundary condition in* (3) *is exact, the reconstructed wavefield* v_R^T *is exactly the complex conjugate of* u^T *in* $\Omega\backslash B$*, i.e.,*

$$v_R^T \equiv \overline{u^T}_{|\Omega\backslash B}.$$

Remark 1.2. Note that Claim 1.1 only holds in the case where trial domain B encloses entirely the inclusion D. If by any chance, the location of B with respect to D is not satisfied, then the reconstruction will not hold independently of the chosen TRAC [17, 18, 53]. ■

1.2 Research questions

The *TRAC* method has already been extensively studied in the time domain [16, 17, 18, 52, 51, 53, 48], but only mentioned quickly in the frequency domain [17, 59]. Time reversal relies on the reversibility in time of the wave equation. Therefore, the first studies never mentioned dissipation or damping, which deprives the equation of the time reversibility. However, in many applications, dissipation is present to some extent and the surrounding medium may not be homogeneous. That is why, we propose to work on the *TRAC* method for more general media.

It is well-known that a damping term in the wave equation gives an attenuated solution over time, modelled by a decreasing exponential. As a result, time reversal of such a term will induce an increasing exponential in the solution. Hence, it is legitimate to wonder if a dissipation can be considered for the *TRAC* method. Since we are working on a finite time frame (in the case of the time-domain wave equation), it is likely that the solution does not have time to blow up and the increasing exponential will not prevent a good reconstruction [60].

Question 1.1. *To which extent does the anti-dissipative term in the* TRAC *method affect the reconstruction of the total (or scattered) wavefield?*

Adding dissipation and working with non-homogeneous[2] media also raises the following question:

Question 1.2. *What can an absorbing boundary condition look like in case of dissipation? and for non-homogeneous media?*

[2]Answers about non-homogeneous media to be seeked in a Part II of this study.

In this paper, we will derive absorbing boundary conditions for dissipative media and observe that the resulting differential operator is hardly translatable from the frequency domain to the time domain via an Inverse Fourier Transform. As a result, a last[3] question comes to mind:

Question 1.3. *If a non-dissipative TRAC problem is considered while there is clear dissipation in the experiment (physical or numeric), how wrong qualitatively and quantitatively is this approximation for the reconstruction of the total (or scattered) wavefield?*

To answer partly to the questions above, we will focus on time-harmonic *TRAC* for the study.

This paper is structured as follows: In Section 2 we propose an analysis in one-space dimension and frequency domain. Explicit calculations will be performed and error quantification will be presented. Then, the two-space dimension case will be illustrated in Section 3 by numerical results. Finally, after the conclusion, two appendices are added: (A) about the derivation of the absorbing boundary conditions and (B) to prove the calculations made in Section 2.

2 Analysis in one-space dimension (and frequency domain)

For this section, we assume that the physical characteristic functions, c (or ε, μ) and σ, are piecewise constant, i.e., constant in the surrounding medium and constant in the inclusion D. Working in one-space dimension reduces the Helmholtz equation to a linear constant coefficient second order ordinary differential equation that can be easily solved by hand to access analytical solutions. Therefore, we show that the *TRAC* method provides exact reconstructions of the total wavefield for the correct location of B with respect to D. We compare these solutions with solutions to classical time reversal that model time reversal physical experiments.

In a second part of this section, we also consider an inexact time reversed absorbing condition on the boundary of B. This consideration is meant to explore how wrong the *TRAC* method can be in presence of dissipation. More precisely, the exact dissipative absorbing condition is hardly translatable in the time-domain. Therefore, we are tempted to use the non-dissipative condition even though we know that the surrounding medium is dissipative. We aim to quantify the error made by this approximation.

2.1 Exact *TRAC* reconstruction in 1D

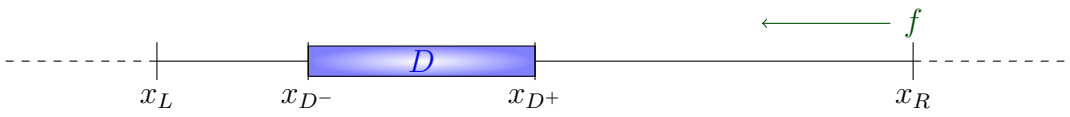

Figure 2: Geometry for the forward problem in 1D: Source f emits a signal in numerically bounded domain $\Omega := [x_L, x_R]$. The wavefield is impinging on inclusion D, delimited by $[x_{D^-}, x_{D^+}]$.

In one-space dimension, see Figure 2, the acoustic total wavefield satisfies:

$$\begin{cases} -\omega^2 u^T + i\omega\sigma(x)u^T - c(x)^2 u^{T\prime\prime} = 0, & \text{in } (x_L, x_R), \\ i\omega_{\sigma_0} u^T - c_0 u^{T\prime} = 0, & \text{on } \{x_L\}, \\ i\omega_{\sigma_0} u^T + c_0 u^{T\prime} = f, & \text{on } \{x_R\}, \end{cases} \tag{4}$$

[3] at least for now in this paper...

where

$$\omega_{\sigma_0} = \omega\sqrt{1 - \frac{i\sigma_0}{\omega}}. \tag{5}$$

The derivation of the boundary conditions is given in Appendix A.1. Problem (4) actually holds for penetrable inclusions, i.e., inclusions that will also let part of the wavefield propagate through itself. For sake of completeness, we consider fully reflective inclusions known as sound-soft and sound-hard as well. The forward problem then reads:

$$\begin{cases} -\omega^2 u^T + i\omega\sigma_0 u^T - c_0^2 u^{T\prime\prime} = 0, & \text{in } (x_L, x_{D^-}) \cup (x_{D^+}, x_R), \\ u^T = 0, & \text{on } \{x_{D^-}\} \cup \{x_{D^+}\} \text{ if sound-soft}, \\ u^{T\prime} = 0, & \text{on } \{x_{D^-}\} \cup \{x_{D^+}\} \text{ if sound-hard}, \\ i\omega_{\sigma_0} u^T - c_0 u^{T\prime} = 0, & \text{on } \{x_L\}, \\ i\omega_{\sigma_0} u^T + c_0 u^{T\prime} = f, & \text{on } \{x_R\}. \end{cases} \tag{6}$$

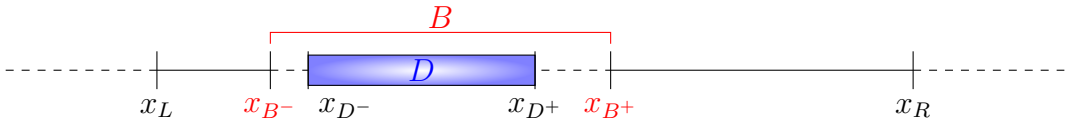

Figure 3: Geometry when performing *TRAC* in 1D: Artificial ball $B = [x_{B^-}, x_{B^+}]$ is introduced and assumed to enclose inclusion D.

Now assume that we record data at $\{x_L\}$ and $\{x_R\}$. An artificial ball $B = [x_{B^-}, x_{B^+}]$ is introduced and assumed to enclose inclusion D, see Figure 3. Now, the computational domain $\Omega\backslash B$ corresponds to the two disconnected segments (x_L, x_{B^-}) and (x_{B^+}, x_R). The *TRAC* problem to reconstruct the total wavefield from measurements satisfies:

$$\begin{cases} -\omega^2 v_R^T - i\omega\sigma_0 v_R^T - c_0^2 v_R^{T\prime\prime} = 0, & \text{in } (x_L, x_{B^-}) \cup (x_{B^+}, x_R), \\ -i\overline{\omega_{\sigma_0}}\, v_R^T - c_0 v_R^{T\prime} = -i\overline{\omega_{\sigma_0}}\, \overline{u^I} - c_0 \overline{u^I}', & \text{on } \{x_{B^-}\}, \\ -i\overline{\omega_{\sigma_0}}\, v_R^T + c_0 v_R^{T\prime} = -i\overline{\omega_{\sigma_0}}\, \overline{u^I} + c_0 \overline{u^I}', & \text{on } \{x_{B^+}\}, \\ v_R^T = \overline{u^T}, & \text{on } \{x_L\} \cup \{x_R\}. \end{cases} \tag{7}$$

Parameter ω_σ in the Helmholtz equation is now complex conjugated and only takes the properties of the surrounding medium. The last line of (7) corresponds to the time reversed measurements. Note that in the case of sound-soft or sound-hard inclusions, the time reversed solution (as well as the forward one) is constant equal to zero in $[x_L, x_{B^-}]$ (as it was in $[x_L, x_{D^-}]$, too). Therefore, for sound-soft or sound-hard inclusions, we solve (7), and compare with the forward reference, only in (x_{B^+}, x_R).

Proposition 2.1. *The general solution to* (7)*, independently of the form of the incident and the total wavefield, is*

$$v_R^T(x) = \begin{cases} \overline{u^T}(x_L) e^{-i\overline{k_{\sigma_0}}(x-x_L)} + \dfrac{\mathrm{TRAC}_{ex}^-[\overline{u^I}](x_{B^-})}{2i\overline{\omega_{\sigma_0}}} \left(e^{-i\overline{k_{\sigma_0}}(x+x_{B^-}-2x_L)} - e^{i\overline{k_{\sigma_0}}(x-x_{B^-})} \right), & \text{if } x \in [x_L, x_{B^-}], \\ \overline{u^T}(x_R) e^{i\overline{k_{\sigma_0}}(x-x_R)} + \dfrac{\mathrm{TRAC}_{ex}^+[\overline{u^I}](x_{B^+})}{2i\overline{\omega_{\sigma_0}}} \left(e^{i\overline{k_{\sigma_0}}(x+x_{B^+}-2x_R)} - e^{-i\overline{k_{\sigma_0}}(x-x_{B^+})} \right), & \text{if } x \in [x_{B^+}, x_R], \end{cases} \tag{8}$$

where operators $\mathrm{TRAC}_{ex}^{\pm}$ *stand for*

$$\mathrm{TRAC}_{ex}^{\pm}[u] := -i\overline{\omega_{\sigma_0}}\, u \pm c_0 u'.$$

Proof. For sake of clarity, see Appendix B.3 for the calculations. □

Corollary 2.1. *If the trial domain encloses the inclusion, solving Problem* (7) *gives the exact reconstruction of the total field, solution to* (4)*, after conjugation, i.e.,*

$$v_R^T \;\equiv\; \overline{u^T}_{|[x_L,x_{B^-}]\cup[x_{B^+},x_R]}.$$

Remark 2.1. In the one-dimension case, an erroneous choice of location for B with respect to D only occurs within $(x_{D^-}, x_{B^-}) \cup (x_{B^+}, x_{D^+})$, where the wavefield propagates inside the inclusion with the physical properties of the surrounding medium. ■

2.2 Classical time reversal reconstruction in 1D

Obviously, the *TRAC* method is a numerical method only. It is not possible to perform *TRAC* on physical experiments. However, we can model time reversal techniques, which we will refer to as Classical Time Reversal, as they would be in physical experiments for the sake of comparison. With measurements on $\{x_L\}$ and $\{x_R\}$, the classical TR problem reads:

$$\begin{cases} -\omega^2\, w_{R,2}^T - i\omega\sigma(x)\, w_{R,2}^T - c(x)^2 {w_{R,2}^T}'' &= 0, & \text{in } (x_L, x_R), \\ w_{R,2}^T &= \overline{u^T}, & \text{on } \{x_L\} \cup \{x_R\}. \end{cases} \tag{9}$$

A similar problem can be written in the case of only one measurement on $\{x_R\}$ and an out-going absorbing boundary condition[4] on $\{x_L\}$

$$\begin{cases} -\omega^2\, w_{R,1}^T - i\omega\sigma(x) w_{R,1}^T - c(x)^2 {w_{R,1}^T}'' &= 0, & \text{in } (x_L, x_R), \\ -i\overline{\omega_\sigma} w_{R,1}^T - c_0 {w_{R,1}^T}' &= 0, & \text{on } \{x_L\}, \\ w_{R,1}^T &= \overline{u^T}, & \text{on } \{x_R\}. \end{cases} \tag{10}$$

Proposition 2.2. *If the scatterer's location and physical characteristics are known (e.g., the inclusion is still present in the computational domain during the experiment), then the solution to* (9) *or* (10) *is exact everywhere in* $[x_L, x_R]$*.*

Proof. We check the result with Maple. The detail of the derivation is fastidious and without much interest as soon as symbolic computing can be used. Therefore, we prefer to skip these calculations here, – refer Appendix B.2 for the calculations.
Note that the result is true independently of the choice of boundary condition at $\{x_L\}$: data or out-going ABC. □

Proposition 2.3. *Assume that we do not know the type and location of the inclusions. Then,* $\sigma(x) = \sigma_0$ *and* $c(x) = c_0$ *by assumption for all* x *in the computational domain. When solving* (9) *and* (10) *under these assumptions, the solutions respectively reads:*

- *two measurements are used, one at* $\{x_L\}$ *and the other at* $\{x_R\}$*, aka* (9)*:*

$$w_{R,2}^T(x) = \frac{\overline{u^T(x_R)}\left(e^{-i\overline{k_{\sigma_0}}(x-x_L)} - e^{i\overline{k_{\sigma_0}}(x-x_L)}\right) + \overline{u^T(x_L)}\left(e^{i\overline{k_{\sigma_0}}(x-x_R)} - e^{-i\overline{k_{\sigma_0}}(x-x_R)}\right)}{e^{-i\overline{k_{\sigma_0}}(x_R-x_L)} - e^{i\overline{k_{\sigma_0}}(x_R-x_L)}}, \quad \forall\, x \in [x_L, x_R].$$

[4] time-reversed, aka. complex conjugated from the forward counterpart.

- *only one measurement at* $\{x_R\}$ *is available, aka* (10)*:*

$$w^T_{R,1}(x) \;=\; \overline{u^T(x_R)}e^{-i\overline{k_{\sigma_0}}(x-x_R)}, \qquad \forall\, x \in [x_L, x_R].$$

Proof. For the sake of clarity, please refer to Appendix B.2.
From the form of the solutions, we can see that only two plane waves travel in both directions, which does not allow for any fluctuations (as in the case of penetrable inclusions) or abrupt reflections (as for sound-soft or sound-hard inclusions). It is then visible that the solutions will differ from the targeted total wavefield after complex conjugation. Note also that this result applies for more than one inclusion of any type as long as $\{x_L\}$ and $\{x_R\}$ are located in the surrounding medium. □

In Figure 4, we display the solutions to the perfect time reversal together with both possible numerical time reversal (9) and (10) when $\sigma(x) = \sigma_0$ and $c(x) = c_0$. We choose the following parameters specified:

- the computational domain is $(x_L, x_R) = (0, 10)$, and the inclusion is located at $(x_{D^-}, x_{D^+}) = (2, 5)$;
- in the surrounding medium $c_0 = 1$ and $\sigma_0 = 0.01$; in the case of a penetrable inclusion, $c_D = 1.5$ and $\sigma_D = 0.2$;
- source term $f = 1$ and frequency $\omega = 5$.

The illustration confirms our incapacity in reconstructing the targeted total wavefield when performing numerical time reversal (unknown inclusions).

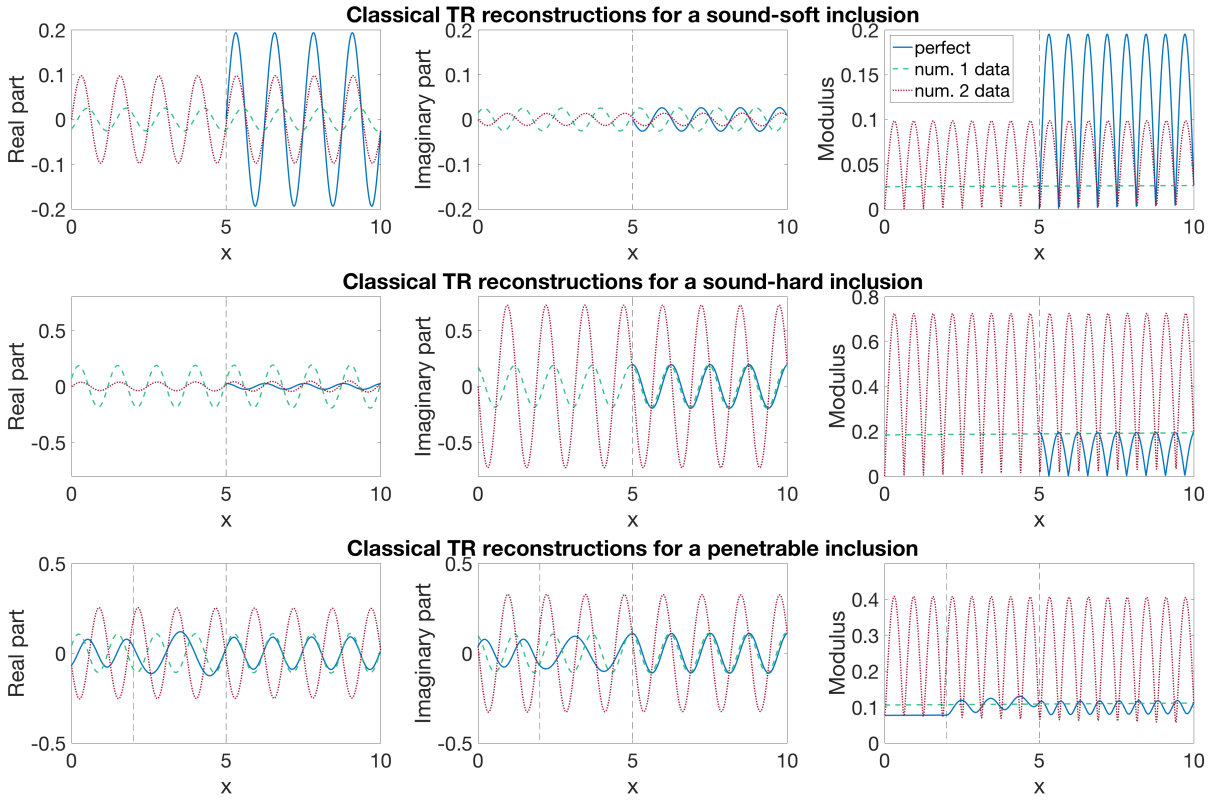

Figure 4: 1D Classical TR – Real part (left), imaginary part (centre) and modulus (right) of the solution to time reversal problems: perfect vs. numerical TR using one measurement vs. numerical TR using two measurements. The dashed vertical lines show the location of the inclusion D.

In some applications, namely in laboratories [6, 1], classical time reversal in the living medium is possible. However, for many (large-scale) applications [5], performing time reversal experiments in real media is not conceivable. Consequently, numerical experiments are used from acquired measurements and inclusions to detect are usually unknown. In that case, classical time reversal cannot be trusted to reconstruct the total (or scattered) wavefield as shown by Proposition 2.3.

2.3 Erroneous *TRAC* reconstruction in 1D

In this paper, we focus our analysis in the frequency domain, since it allows for analytical solutions and exact calculations. However, the underlying idea is to study the effect of an approximate non-dissipative time reversed absorbing boundary condition when dissipation is involved in the forward problem. We can already see that the exact absorbing boundary condition in 1D and frequency domain is hardly translatable to the time domain, hence the need for an approximation of the absorbing boundary condition and a quantification of the inherent error. Some details of the calculations are available in Appendix B.3.

We will compare three levels of approximation to the exact TRAC problem (7):

- 1^{st}-order approximation of the time-reversed ABC, aka 'approx.' TRAC

$$-i\overline{\omega_\sigma} := -i\omega\sqrt{1+\frac{i\sigma_0}{\omega}} \simeq -i\omega + \frac{\sigma_0}{2}, \qquad \text{for very small values of } \sigma_0.$$

- omission of the dissipation in the time-reversed ABC (or 0^{th}-order), aka 'wrong' TRAC

$$-i\overline{\omega_\sigma} := -i\omega\sqrt{1+\frac{i\sigma_0}{\omega}} \approx -i\omega.$$

- omission of the dissipation in the entire TRAC problem, aka 'very wrong' TRAC

$$\overline{\omega_\sigma} \approx \omega, \quad \text{everywhere.}$$

Let's take the following notation for the absorbing boundary conditions:

$$\mathrm{TRAC}^{\pm}_{0th}[u] := -i\omega\, u \pm c_0 u', \tag{11}$$

$$\text{and} \quad \mathrm{TRAC}^{\pm}_{1st}[u] := \left(-i\omega + \frac{\sigma_0}{2}\right) u \pm c_0 u' \tag{12}$$

Proposition 2.4. The 'approx.' TRAC case:
A first-order approximation to the TRAC problem can be written as:

$$\begin{cases} -\omega^2 v^T_{R,approx} - i\omega\sigma_0 v^T_{R,approx} - c_0^2 {v^T_{R,approx}}'' &= 0, & \text{in } (x_L, x_{B^-}) \cup (x_{B^+}, x_R), \\ \mathrm{TRAC}^-_{1st}[v^T_{R,approx}] &= \mathrm{TRAC}^-_{1st}[\overline{u^I}], & \text{on } \{x_{B^-}\}, \\ \mathrm{TRAC}^+_{1st}[v^T_{R,approx}] &= \mathrm{TRAC}^+_{1st}[\overline{u^I}], & \text{on } \{x_{B^+}\}, \\ v^T_{R,approx} &= \overline{u^T}, & \text{on } \{x_L\} \cup \{x_R\}. \end{cases} \tag{13}$$

The general solution is:

$$v^T_{R,approx}(x) = \begin{cases} \frac{1}{\Psi}\left[\overline{u^T}(x_L)\left(\left(i(\overline{\omega_{\sigma_0}}+\omega)-\frac{\sigma_0}{2}\right)e^{-i\overline{k_{\sigma_0}}(x-x_{B^-})}+\left(i(\overline{\omega_{\sigma_0}}-\omega)+\frac{\sigma_0}{2}\right)e^{i\overline{k_{\sigma_0}}(x-x_{B^-})}\right)\right. \\ \qquad \left.+\mathrm{TRAC}^-_{1st}[\overline{u^I}](x_{B^-})\left(e^{-i\overline{k_{\sigma_0}}(x-x_L)}-e^{i\overline{k_{\sigma_0}}(x-x_L)}\right)\right], & \text{if } x\in[x_L,x_{B^-}], \\ \frac{1}{\Phi}\left[\overline{u^T}(x_R)\left(\left(i(\overline{\omega_{\sigma_0}}-\omega)+\frac{\sigma_0}{2}\right)e^{-i\overline{k_{\sigma_0}}(x-x_{B^+})}+\left(i(\overline{\omega_{\sigma_0}}+\omega)-\frac{\sigma_0}{2}\right)e^{i\overline{k_{\sigma_0}}(x-x_{B^+})}\right)\right. \\ \qquad \left.+\mathrm{TRAC}^+_{1st}[\overline{u^I}](x_{B^+})\left(e^{i\overline{k_{\sigma_0}}(x-x_R)}-e^{-i\overline{k_{\sigma_0}}(x-x_R)}\right)\right], & \text{if } x\in[x_{B^+},x_R], \end{cases} \tag{14}$$

with

$$\Phi = \left(i(\overline{\omega_{\sigma_0}}-\omega)+\frac{\sigma_0}{2}\right)e^{i\overline{k_{\sigma_0}}(x_{B^+}-x_R)}+\left(i(\overline{\omega_{\sigma_0}}+\omega)-\frac{\sigma_0}{2}\right)e^{-i\overline{k_{\sigma_0}}(x_{B^+}-x_R)}$$

$$\text{and}\quad \Psi = \left(i(\overline{\omega_{\sigma_0}}+\omega)-\frac{\sigma_0}{2}\right)e^{i\overline{k_{\sigma_0}}(x_{B^-}-x_L)}+\left(i(\overline{\omega_{\sigma_0}}-\omega)+\frac{\sigma_0}{2}\right)e^{-i\overline{k_{\sigma_0}}(x_{B^-}-x_L)}.$$

For the sake of illustration, we use the following parameters: $f=1$, $\omega=5$, $(x_L,x_R)=(0,10)$, $(x_{D^-},x_{D^+})=(2,5)$, $(x_{B^-},x_{B^+})=(1.5,6)$, and $c_0=1$, $\sigma_0=0.7$, $c_D=1.5$, $\sigma_D=2$. In Figure 5, we plot the complex conjugated total wavefield for reference, together with the exact TRAC reconstruction (8) and the approximated TRAC reconstruction (14). We observe that all three curves are superimposed in $(x_L,x_{B^-})\cup(x_{B^+},x_R)$ for this choice of parameters, which also reveals that (14) gives a very good approximation. The error will be quantified in a latter section.

Proposition 2.5. The 'wrong' TRAC case:
A zero-th-order approximation (omitting dissipation on the absorbing boundary conditions) to the TRAC problem can be written as:

$$\begin{cases} -\omega^2 v^T_{R,wrong} - i\omega\sigma_0 v^T_{R,wrong} - c_0^2 {v^T_{R,wrong}}'' &=& 0, & \text{in } (x_L,x_{B^-})\cup(x_{B^+},x_R), \\ \mathrm{TRAC}^-_{0th}[v^T_{R,wrong}] &=& \mathrm{TRAC}^-_{0th}[\overline{u^I}], & \text{on } \{x_{B^-}\}, \\ \mathrm{TRAC}^+_{0th}[v^T_{R,wrong}] &=& \mathrm{TRAC}^+_{0th}[\overline{u^I}], & \text{on } \{x_{B^+}\}, \\ v^T_{R,wrong} &=& \overline{u^T}, & \text{on } \{x_L\}\cup\{x_R\}. \end{cases} \tag{15}$$

The general solution is:

$$v^T_{R,wrong}(x) = \begin{cases} \frac{1}{\Xi}\left[\overline{u^T}(x_L)\left((\overline{\omega_{\sigma_0}}+\omega)e^{-i\overline{k_{\sigma_0}}(x-x_{B^-})}+(\overline{\omega_{\sigma_0}}-\omega)e^{i\overline{k_{\sigma_0}}(x-x_{B^-})}\right)\right. \\ \qquad \left.+\,i\,\mathrm{TRAC}^-_{0th}[\overline{u^I}](x_{B^-})\left(e^{i\overline{k_{\sigma_0}}(x-x_L)}-e^{-i\overline{k_{\sigma_0}}(x-x_L)}\right)\right], & \text{if } x\in[x_L,x_{B^-}], \\ \frac{1}{\Theta}\left[\overline{u^T}(x_R)\left((\overline{\omega_{\sigma_0}}-\omega)e^{-i\overline{k_{\sigma_0}}(x-x_{B^+})}+(\overline{\omega_{\sigma_0}}+\omega)e^{i\overline{k_{\sigma_0}}(x-x_{B^+})}\right)\right. \\ \qquad \left.+\,i\,\mathrm{TRAC}^+_{0th}[\overline{u^I}](x_{B^+})\left(e^{-i\overline{k_{\sigma_0}}(x-x_R)}-e^{i\overline{k_{\sigma_0}}(x-x_R)}\right)\right], & \text{if } x\in[x_{B^+},x_R], \end{cases} \tag{16}$$

with

$$\Theta = (\overline{\omega_{\sigma_0}}-\omega)e^{i\overline{k_{\sigma_0}}(x_{B^+}-x_R)}+(\overline{\omega_{\sigma_0}}+\omega)e^{-i\overline{k_{\sigma_0}}(x_{B^+}-x_R)}$$

$$\text{and}\quad \Xi = (\overline{\omega_{\sigma_0}}+\omega)e^{i\overline{k_{\sigma_0}}(x_{B^-}-x_L)}+(\overline{\omega_{\sigma_0}}-\omega)e^{-i\overline{k_{\sigma_0}}(x_{B^-}-x_L)}.$$

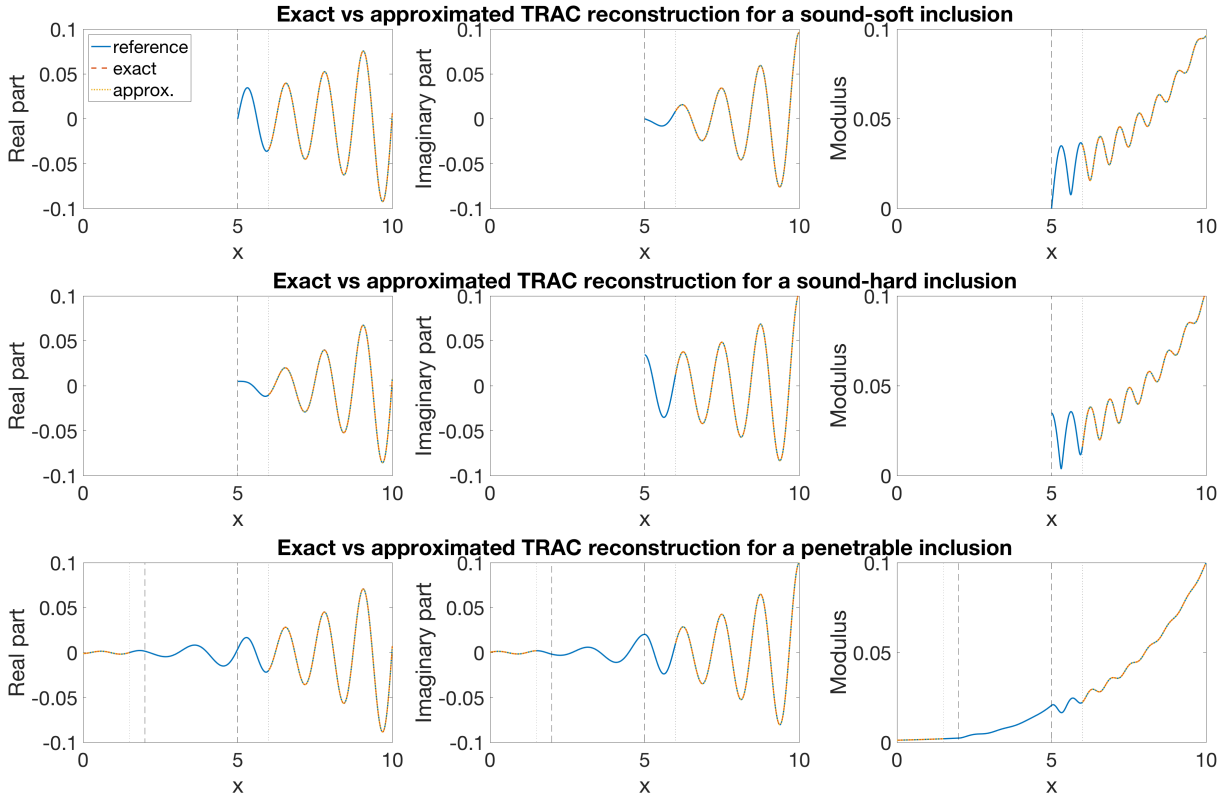

Figure 5: 1D approximated TRAC – Real part (left), imaginary part (centre) and modulus (right) of the solution to time reversal problems: complex conjugated vs. exact TRAC vs. 1^{st}-order approximated TRAC. The dashed vertical lines show the location of the inclusion D. The dotted vertical lines show the location of the artificial domain B.

And finally, we propose to compute the reconstruction using the standard TRAC method, which does not contain any dissipation term.

Proposition 2.6. The 'very wrong' TRAC case:
In the eventuality that the dissipation is unknown altogether, the erroneous TRAC problem becomes:

$$\begin{cases} -\omega^2 v^T_{R,very} - c_0^2 v^T_{R,very}{}'' = 0, & \text{in } (x_L, x_{B^-}) \cup (x_{B^+}, x_R), \\ \text{TRAC}^-_{0th}[v^T_{R,very}] = \text{TRAC}^-_{0th}[\overline{u^I}], & \text{on } \{x_{B^-}\}, \\ \text{TRAC}^+_{0th}[v^T_{R,very}] = \text{TRAC}^+_{0th}[\overline{u^I}], & \text{on } \{x_{B^+}\}, \\ v^T_{R,very} = \overline{u^T}, & \text{on } \{x_L\} \cup \{x_R\}. \end{cases} \tag{17}$$

The general solution is:

$$v^T_{R,very}(x) = \begin{cases} \overline{u^T}(x_L)e^{-ik_0(x-x_L)} + \frac{1}{2i\omega}\text{TRAC}^-_{0th}[\overline{u^I}](x_{B^-})\left(e^{-ik_0(x+x_{B^-}-2x_L)} - e^{ik_0(x-x_{B^-})}\right), & \text{if } x \in [x_L, x_{B^-}], \\ \overline{u^T}(x_R)e^{ik_0(x-x_R)} + \frac{1}{2i\omega}\text{TRAC}^+_{0th}[\overline{u^I}](x_{B^+})\left(e^{ik_0(x+x_{B^+}-2x_R)} - e^{-ik_0(x-x_{B^+})}\right), & \text{if } x \in [x_{B^+}, x_R]. \end{cases} \tag{18}$$

With the same parameters as before, we display in Figure 6 the reference solution together with the 'wrong' TRAC reconstruction (16) and the 'very wrong' one (18). Although the 'wrong' solution seems to give an acceptable reconstruction (some discrepancy is still visible), it is clear that the 'very wrong' one is not reliable at all.

The TRAC method in the presence of dissipation requires a anti-dissipative term in the Helmholtz equation to be valid. We observe that, despite the anti-dissipative component, the solutions to the different variations of the TRAC method do not blow up or increase exponentially in a way preventing the reconstruction.

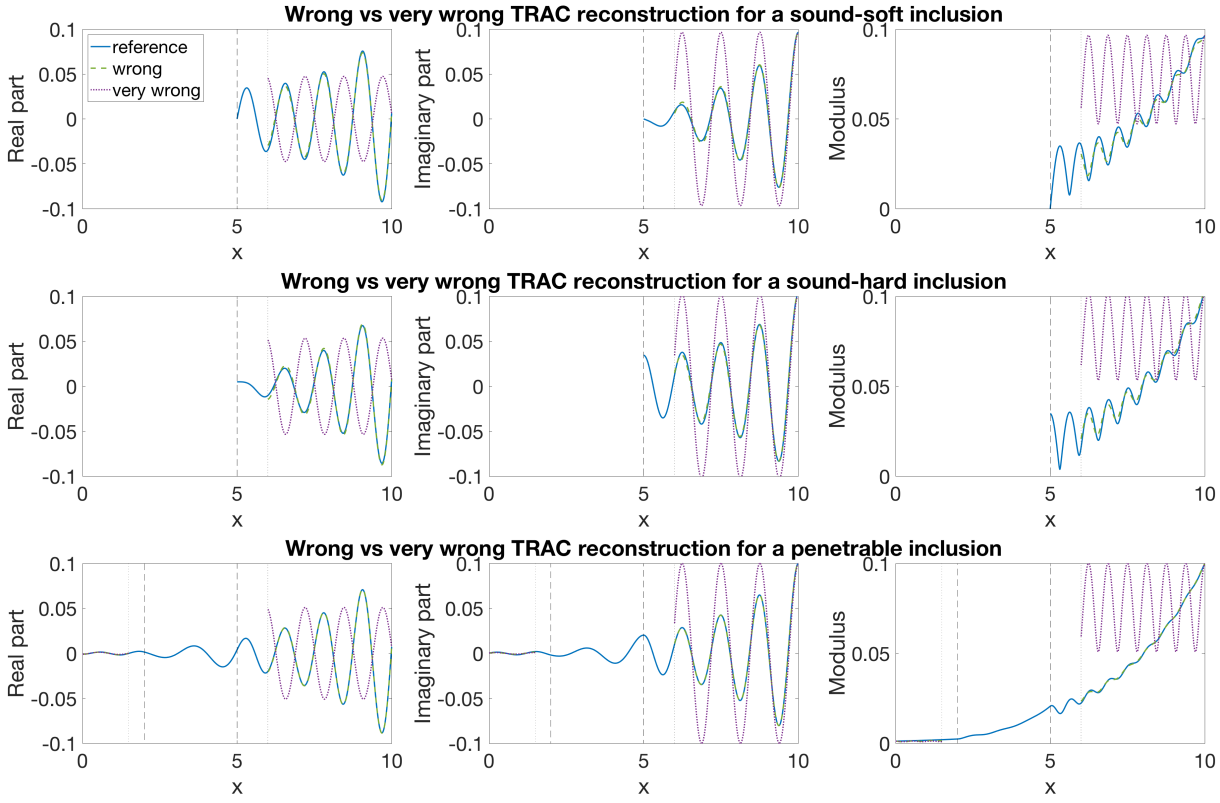

Figure 6: 1D erroneous TRAC – Real part (left), imaginary part (centre) and modulus (right) of the solution to time reversal problems: complex conjugated vs. 'wrong' TRAC vs. 'very wrong' TRAC. The dashed vertical lines show the location of the inclusion D. The dotted vertical lines show the location of the artificial domain B.

2.4 Relative L^2-error of *TRAC* reconstructions in 1D

In this section, we propose to quantify the error made when one of the three erroneous TRAC methods is used instead of the exact one. The motivation is again that the term $i\omega_{\sigma_0}$ does not provide a differential operator after inverse Fourier transform if we wish to transpose the TRAC method with dissipation to the time domain. As a result, some approximations have been proposed and we want to estimate the discrepancy between the targeted wavefield and the reconstructed one.

To make the formulae more digest, we consider the following complex conjugated incident wave

$$\overline{u^I}(x) = -\frac{f}{2i\overline{\omega_{\sigma_0}}} e^{-i\overline{k_{\sigma_0}}(x-x_R)}.$$

The explicit TRAC operators are described in Appendix B.4 and will be used for the rest of this section.

For each approximation of the TRAC methods, we can write the explicit absolute error formula:

- 'Approx.' TRAC

$$E_{approx}(x) = v_R^T(x) - v_{R,approx}^T(x)$$
$$= \begin{cases} \frac{i(\overline{\omega_{\sigma_0}}-\omega)+\frac{\sigma_0}{2}}{\Psi}\left(\overline{u^T}(x_L)\left(e^{-i\overline{k_{\sigma_0}}(x+x_{B^-}-2x_L)}-e^{i\overline{k_{\sigma_0}}(x-x_{B^-})}\right)\right. \\ \left. \quad + \frac{f}{2i\overline{\omega_{\sigma_0}}}\left(e^{-i\overline{k_{\sigma_0}}(x+x_{B^-}-x_R-x_L)}-e^{i\overline{k_{\sigma_0}}(x-x_{B^-}+x_R-x_L)}\right)\right), \quad \text{for } x\in[x_L,x_{B^-}], \\ \frac{i(\overline{\omega_{\sigma_0}}-\omega)+\frac{\sigma_0}{2}}{\Phi}\left(\overline{u^T}(x_R)+\frac{f}{2i\overline{\omega_{\sigma_0}}}\right)\left(e^{i\overline{k_{\sigma_0}}(x+x_{B^+}-2x_R)}-e^{-i\overline{k_{\sigma_0}}(x-x_{B^+})}\right), \\ \qquad\qquad \text{for } x\in[x_{B^+},x_R]. \end{cases} \tag{19}$$

- 'Wrong' TRAC

$$E_{wrong}(x) = v_R^T(x) - v_{R,wrong}^T(x)$$
$$= \begin{cases} \frac{(\overline{\omega_{\sigma_0}}-\omega)}{\Xi}\left(\overline{u^T}(x_L)\left(e^{-i\overline{k_{\sigma_0}}(x+x_{B^-}-2x_L)}-e^{i\overline{k_{\sigma_0}}(x-x_{B^-})}\right)\right. \\ \left. \quad + \frac{f}{2i\overline{\omega_{\sigma_0}}}\left(e^{-i\overline{k_{\sigma_0}}(x+x_{B^-}-x_R-x_L)}-e^{i\overline{k_{\sigma_0}}(x-x_{B^-}+x_R-x_L)}\right)\right), \quad \text{for } x\in[x_L,x_{B^-}], \\ \frac{(\overline{\omega_{\sigma_0}}-\omega)}{\Theta}\left(\overline{u^T}(x_R)+\frac{f}{2i\overline{\omega_{\sigma_0}}}\right)\left(e^{i\overline{k_{\sigma_0}}(x+x_{B^+}-2x_R)}-e^{-i\overline{k_{\sigma_0}}(x-x_{B^+})}\right), \\ \qquad\qquad \text{for } x\in[x_{B^+},x_R]. \end{cases} \tag{20}$$

- 'Very wrong' TRAC

$$E_{very}(x) = v_R^T(x) - v_{R,very}^T(x)$$
$$= \begin{cases} \overline{u^T}(x_L)\left(e^{-i\overline{k_{\sigma_0}}(x-x_L)}-e^{-ik_0(x-x_L)}\right) \\ \quad + \frac{f\,e^{-i\overline{k_{\sigma_0}}(x_{B^-}-x_R)}}{2i\overline{\omega_{\sigma_0}}}\frac{(\overline{\omega_{\sigma_0}}-\omega)}{2\omega}\left(e^{-ik_0(x+x_{B^-}-2x_L)}-e^{ik_0(x-x_{B^-})}\right), \quad \text{for } x\in[x_L,x_{B^-}], \\ \overline{u^T}(x_R)\left(e^{i\overline{k_{\sigma_0}}(x-x_R)}-e^{ik_0(x-x_R)}\right)-\frac{f}{2i\overline{\omega_{\sigma_0}}}\left(e^{-i\overline{k_{\sigma_0}}(x-x_R)}-e^{i\overline{k_{\sigma_0}}(x-x_R)}\right) \\ \quad + \frac{f\,e^{-i\overline{k_{\sigma_0}}(x_{B^+}-x_R)}}{2i\overline{\omega_{\sigma_0}}}\frac{(\overline{\omega_{\sigma_0}}+\omega)}{2\omega}\left(e^{-ik_0(x-x_{B^+})}-e^{ik_0(x+x_{B^+}-2x_R)}\right), \quad \text{for } x\in[x_{B^+},x_R]. \end{cases} \tag{21}$$

By deriving the error formulae in the case of our three usual types of inclusion, we obtain the following result:

Proposition 2.7. *For the* 1*st-order approximation and the* 0*th-order approximation of the TRAC method, the error in the case of a sound-soft inclusion is the opposite of the error in the case of a sound-hard inclusion at the same location and with the same settings, for all* $x \in [x_{B^+}, x_R]$.
However, we cannot conclude for the variant without dissipation.

Proof. The calculations were made with Maple and can be easily derived using Appendices B.3 and B.4. □

Conjecture 2.1. *For the* 1*st-order approximation and the* 0*th-order approximation of the TRAC method, the modulus of the error in the case of a penetrable inclusion is smaller or equal than*

the modulus of the error in the case of a sound-hard inclusion at the same location and with the same settings (and for any values of the penetrable inclusion).

$$|E^{penetrable}(x)| \leq |E^{hard}(x)| = |E^{soft}(x)|, \qquad \forall\, x \in [x_{B^+}, x_R].$$

If the statement above is correct, then we can deduce the behaviour of the error by considering the case of a sound-soft (or sound-hard) only, provided that all tests are using inclusions at the same location and with the same settings.

Remark 2.2. To prove Conjecture 2.1, we need to show that

$$\frac{|E^{penetrable}(x)|}{|E^{hard}(x)|} = \left| \frac{(\overline{k_{\sigma_D}}^2 - \overline{k_{\sigma_0}}^2)\left(e^{-2i\overline{k_{\sigma_D}}x_{D^-}} - e^{-2i\overline{k_{\sigma_D}}x_{D^+}}\right)}{(\overline{k_{\sigma_D}} + \overline{k_{\sigma_0}})^2 e^{-2i\overline{k_{\sigma_D}}x_{D^+}} - (\overline{k_{\sigma_D}} - \overline{k_{\sigma_0}})^2 e^{-2i\overline{k_{\sigma_D}}x_{D^-}}} \right| \leq 1.$$

We have not managed to prove it, nor to find a counter-example. The question is still open. ■

In Figure 7, we display the absolute errors for the following parameters: $f = 1$, $\omega = 5$, $(x_L, x_R) = (0, 10)$, $(x_{D^-}, x_{D^+}) = (2, 5)$, $(x_{B^-}, x_{B^+}) = (1.5, 6)$, and $c_0 = 1$, $\sigma_0 = 0.01$, $c_D = 1.5$, $\sigma_D = 2$. We observe that the results in Proposition 2.7 are satisfied. Moreover, we clearly see that the 1^{st}-order approximation performs much better than the two others, with an error bounded by 5×10^{-8} for 'approx.', by 10^{-4} for 'wrong' and 5×10^{-3} for 'very wrong'. Note that the error is particularly good because we took a small σ_0. For instance, if we now consider $\sigma_0 = 0.7$ (the other parameters remain the same), then the error increases for the three approximated TRAC problems: the error is bounded by 3×10^{-4} for 'approx.', by 6×10^{-3} for 'wrong' and 0.2 for 'very wrong'.

Finally, we are interested in the behaviour of the error as a function of the ambient dissipation σ_0, so that we can determine the values of σ_0 for which the error is negligible or, on the contrary, that will give a very poor reconstruction. We consider the relative L^2-error for this study

$$e_{variant}(\sigma_0) := \frac{\|E_{variant}\|_{L^2}}{\|v_R^T\|_{L^2}},$$

where *variant* refers to the different possible approximations of the TRAC method listed above and we recall that v_R^T is the exact TRAC reconstruction. Note that the L^2-norm is taken either in $[x_L, x_{B^-}]$ or in $[x_{B^+}, x_R]$, since the behaviour differs on each interval. In particular, for sound-soft or sound-hard inclusions (in the current settings), the reconstruction only occurs in $[x_{B^+}, x_R]$.

For the numerical test, we consider the same parameters as for Figure 7, except that σ_0 varies in $[0, 10]$ and in $[0, 100]$. In Figure 8, we display the relative L^2-error calculated on the interval $[x_{B^+}, x_R]$. We compare the error for the different types of inclusions. From the top row zooming-in for values of $\sigma_0 \in [0, 10]$, the relative L^2-error clearly has a maximum and then seems to converge towards zero at the infinity for the 'approx' and the 'wrong' TRAC methods. However, for the 'very wrong' TRAC method, we see a strictly increasing error, which confirms that the standard TRAC method (omitting any dissipation) is not reliable. For other two methods, we seek for the value of σ_0 giving the maximal error and the range of values for σ_0 so that the relative L^2-error is below 1%. Note that the error is having its maximum for the same value of σ_0 independently of the type of inclusion. We summarise the results in Table 1.

While zooming-out, see bottom row of Figure 8, we actually realise that our conjecture on the behaviour of the error for large values of σ_0 was wrong. It rather seems to reach a point where the error is 100% and stagnates at this value. Therefore, it seems that below a given value

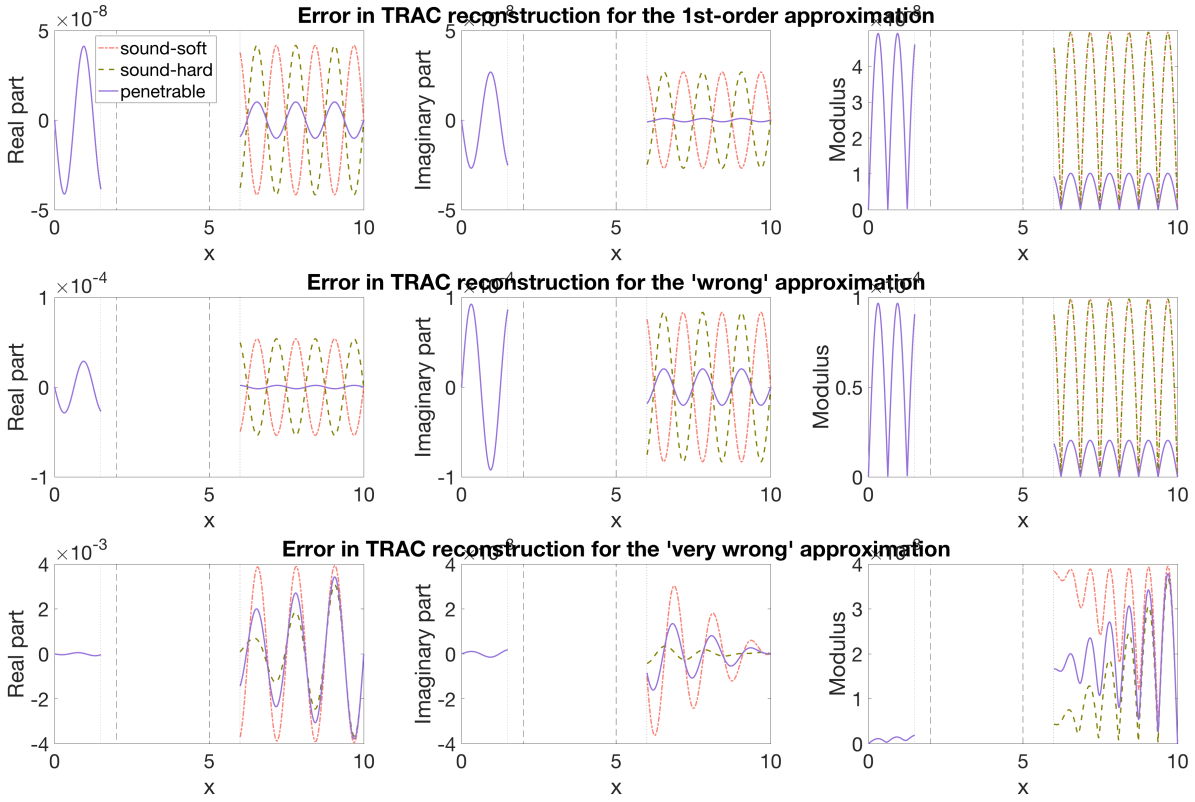

Figure 7: 1D approximated TRAC – Real part (left), imaginary part (centre) and modulus (right) of the absolute error: 1^{st}-order approximated TRAC ('approx', top row), 0^{th}-order approximated TRAC ('wrong', middle row) and standard TRAC without dissipation ('very wrong', bottom row). The dashed vertical lines show the location of the inclusion D. The dotted vertical lines show the location of the artificial domain B.

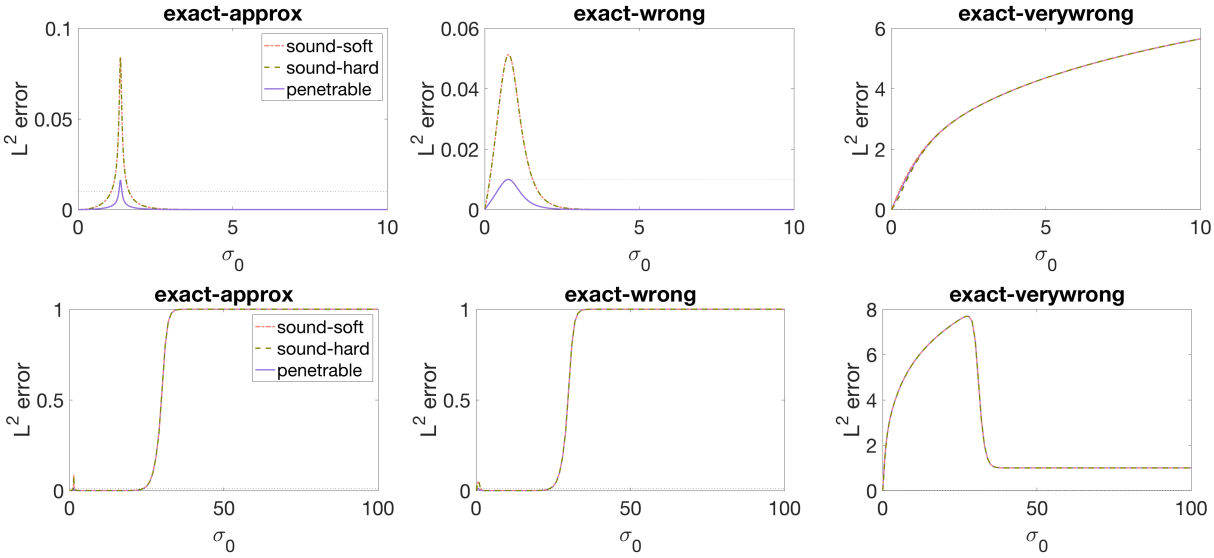

Figure 8: 1D approximated TRAC – Relative L^2-error between the approximations of the TRAC method and the exact dissipative TRAC, computed in $[x_{B^+}, x_R]$: 1^{st}-order approximated TRAC ('approx', left), 0^{th}-order approximated TRAC ('wrong', centre) and standard TRAC without dissipation ('very wrong', right). The dotted horizontal line shows the 1% threshold. The bottom row is a zoom-out of the top row for a wider range of σ_0.

method/$\sigma_0 < 10$	$< 1\%$ before max	max	$< 1\%$ after max
'approx'	$<\sim 1.07$	~ 1.36	$>\sim 1.65$
'wrong'	$<\sim 0.53$	~ 0.77	$>\sim 1.56$
'very wrong'	$<\sim 0.0043$	$\emptyset$	$\emptyset$

Table 1: 1D approximated TRAC – Relative L^2-error between the approximations of the TRAC method and the exact dissipative TRAC, computed in $[x_{B^+}, x_R]$: values of σ_0 which give a maximum or an error below 1%, for the parameters of the numerical experiments $f = 1$, $\omega = 5$, $(x_L, x_R) = (0, 10)$, $(x_{D^-}, x_{D^+}) = (2, 5)$, $(x_{B^-}, x_{B^+}) = (1.5, 6)$, and $c_0 = 1$, $c_D = 1.5$, and $\sigma_D = 2$. Only values of $\sigma_0 < 10$ are considered (Zoom-in).

of σ_0, the error is acceptable and suddenly the approximation is not good enough to trust the reconstruction.

Finally, we show the relative L^2-error calculated in the interval $[x_L, x_{B^-}]$ (for penetrable inclusions only) in Figure 9. Overall, the error seems to increase less than in the other interval, perhaps because the wavefield has been damped a lot while passing through the inclusion. We also conjecture a convergence toward 100% as σ_0 goes to infinity, which is consistent with the results shown in Figure 8.

Remark 2.3. The observations made above concerned this specific test with the chosen parameters. However, it seems that the global behaviour remains even with other sets of parameters. Unfortunately, this has not been proven yet, as the formulae for the relative L^2-error with respect to σ_0 could not be explicit and analysed. ■

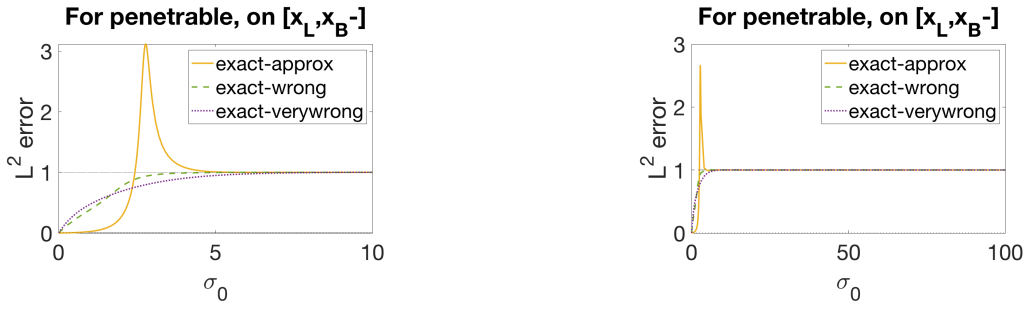

Figure 9: 1D approximated TRAC – Relative L^2-error between the approximations of the TRAC method and the exact dissipative TRAC, computed in $[x_L, x_{B^-}]$ (penetrable inclusion only). The dotted horizontal line shows the 1% threshold, while the dashed horizontal line represents 100% error. The right picture is a zoom-out of the left one for a wider range of σ_0.

3 Numerical experiments in two-space dimensions (and frequency domains)

As it is well known, 2D is not the best candidate for exact formulations. Therefore, we do not present any proof for Claim 1.1. However, a good approximation for the absorbing boundary condition may induce a good enough reconstruction of the total (or scattered) wavefield. For the first studies on the *TRAC* method, the first order Bayliss-Turkel boundary condition was used successfully for elliptic trial domain [16, 17, 18]. More recently, the second order Enquist-Madja boundary condition was also proposed in [53] with excellent results, as well.

In this section, we follow [17] and [53], and consider both a first-order Bayliss-Turkel-like absorbing boundary condition and a second-order Engquist-Madje-like ABC to perform the *TRAC* method in 2D in dissipative (and non-homogeneous) media.

3.1 A numerical experiment in 2D – Forward problem

To illustrate the feasibility of the *TRAC* method with dissipation in two-space dimension and frequency domain, we propose a benchmark example. For this, we assume that the surrounding medium is constant and homogeneous, but contains a dissipative component. Also, we use the Helmholtz equation with parameters from electromagnetism: electric permittivity ε, magnetic permeability μ and electric conductivity σ, see Remark 1.1. Furthermore, we denote by ε_0 and μ_0 the electric permittivity and the magnetic permeability, respectively, in the vacuum.

Consider a square computational domain Ω, which contains one or several inclusions. We assume that the surrounding medium is homogeneous and has a relative permittivity $\varepsilon_r = 5$, a relative permeability $\mu_r = 1$ and an electric conductivity $\sigma_0 = \exp(-3) \sim 0.05$. These values correspond to the permittivity, permeability and conductivity of the soil [61]. The size of Ω is taken as $2m$ in width and $2m$ in depth. The inclusions are located somewhere around the centre of Ω.

To solve the forward problem,

$$-\omega^2 \mu_0 \mu_r \left(\omega \varepsilon_0 \varepsilon_r - i\sigma_0\right) u^T - \Delta u^T \;=\; f, \qquad \text{in } \Omega, \tag{22}$$

we use the Finite Element method through the software FreeFem++ [62], namely $\mathbb{P}^2$ elements, and the total-field/scattered-field (TF/SF) formulation [56, 57] with 2^{nd}-order Engquist-Madja boundary conditions. A point source is modelled by

$$f(x,y) \;=\; \frac{i}{4} \cdot H_0^{(2)}(\mathrm{Re}(ik_\sigma \sqrt{(x-x_s)^2 + (y-y_s)^2}) \cdot e^{(-\mathrm{Im}(ik_\sigma)\sqrt{(x-x_s)^2+(y-y_s)^2})}, \tag{23}$$

where $H_0^{(2)}$ is the 0^{th}-order Hankel function of Type 2, (x_s, y_s) are the coordinates of the point source and $k_\sigma := \sqrt{\omega \mu_0 \mu_r \left(\omega \varepsilon_0 \varepsilon_r - i\sigma_0\right)}$.

We work with different types of inclusions, still following the parameters from [61]:

- sound-hard, with $\varepsilon_r = 1$, $\mu_r = 10^4$ and $\sigma = 10^7$. These would for instance correspond to iron mines buried in the land;
- penetrable, with $\varepsilon_r = 3$, $\mu_r = 1$ and $\sigma = 0$, to model mines with plastic wrapping.

We also consider two sizes for the inclusions: a small one with $10 \times 4cm^2$ and a large one with $60 \times 10cm^2$.

In Figure 10, we show the numerical results for the forward problem in the case of three inclusions. We take a computational domain $\Omega = [-1,1] \times [-1,1]$ and the point source is located at $(0.3, 2)$, deliberately slightly uncentered to avoid a perfect alignment of all the components, Figure 10(b). The ambient (or surrounding) medium considered is soil and, of the three inclusions, we look at two small iron mines (centered at $(0.2, 0)$ and $(0, -0.2)$, respectively) and a larger plastic mine enclosing one of the small ones, see Figure 10(a). The large inclusion is centered in the computational domain. We display the total wavefield computed using the TF/SF formulation, with a layer wide of 0.2, in Figure 10(c), where the scattering due to the inclusions is clearly identifiable, and the associate scattered field, obtained by subtracting the incident wave to the total field, is shown in Figure 10(d). We observe all contributions from the three inclusions.

Let's now assume that we record the scattered wavefield on a square receivers' array (boundary of $[-0.78, 0.78] \times [-0.78, 0.78]$, i.e., slightly inside the region where the total field was computed), i.e., here we consider a receivers' array with full aperture and continuous, $\Gamma = \partial\Omega$. From these measurements, we will perform Time Reversal using the *TRAC* method.

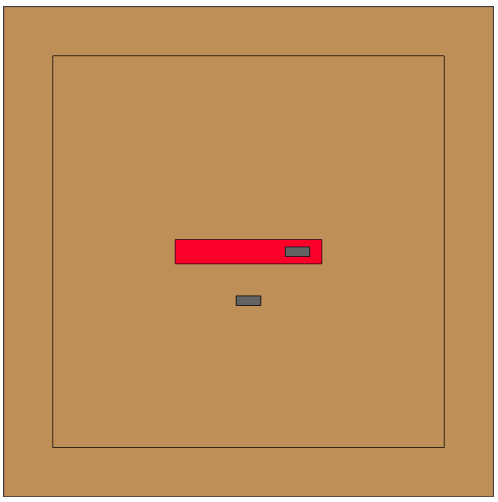

(a) Geometry with three inclusions enclosed in the surrounding medium

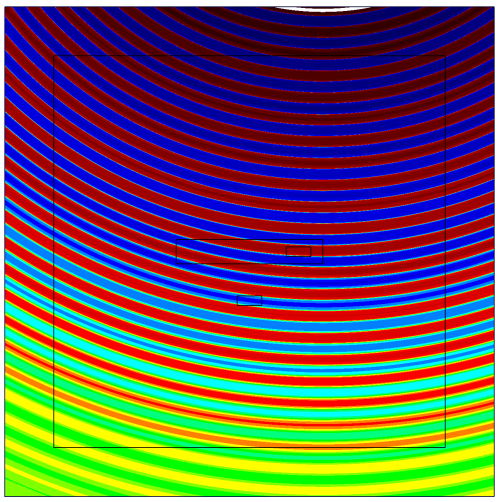

(b) Point source slightly offset, with dissipation $\sigma_0 = \exp(-3)$, (real part)

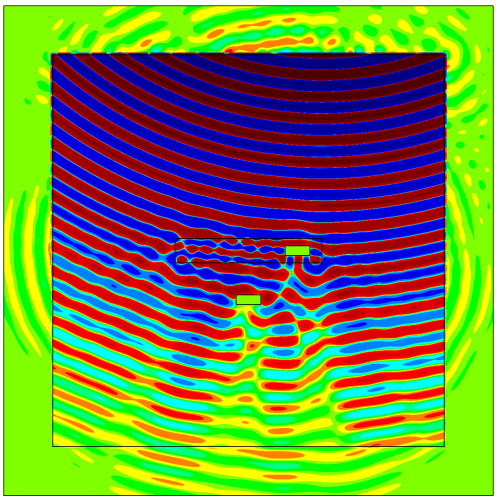

(c) Total wavefield (real part), solved by TF/SF formulation

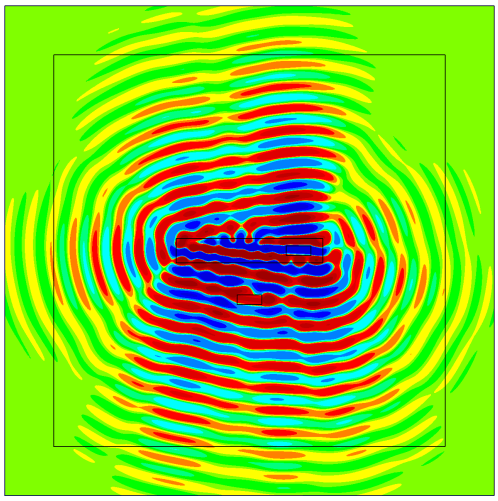

(d) Scattered wavefield (real part), i.e., difference between the incident and total fields

Figure 10: Numerical experiment in 2D – Forward problem: Presentation of the geometry and the resulting wavefields.

3.2 A quick analogy to the 1D case

Before we present the numerical results of the *TRAC* method with the dissipative component, we propose a quick analog analysis in 1D to determine the potential problematic values of σ_0 in terms of accuracy of the reconstruction. To do so, we consider the case of one small sound-hard inclusion located at the centre of the computational domain. To perform TRAC, we introduce a trial ball enclosing the inclusion, as in Figure 11.

In Figure 12, we plot the obtained relative L^2-error for this 1D analog version of the 2D problem. We propose the three possible approximations, but really consider only the two on the left and centred columns. The right column presents the case of the standard TRAC, that we will not consider here. On the top row, we have a view for a large range of σ_0 and we clearly see that from $\sigma_0 \approx 0.75$, the error increases drastically up to 100%. As a result, we'd rather work with values of the dissipation that are much smaller than 0.75. Moreover, a zoom-in allows us to see a specific behaviour of the error for small values of the dissipation. We notice again

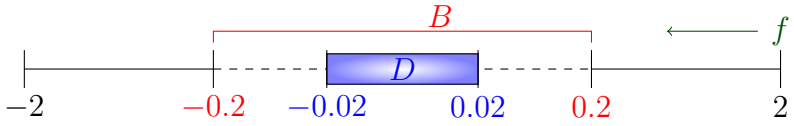

Figure 11: Analogy 1D for the 2D problem aiming at estimating the values of σ_0 potentially giving good reconstructions or very erroneous ones. The graph is not scaled!

a maximum at about 0.034. Note that for the forward problem proposed in Section 3.1, the dissipation in the soil was $\exp(-3) \sim 0.05$, which is beyond that maximum. From the graphs, it seems that the error decays but we cannot yet assess if this is only a result for the 1D case and if this can be transposed in 2D. More precisely, we can expect that the error increases for values of $\sigma_0 < 0.034$, but it may be that the error does not necessarily decrease sufficiently for larger values to give a satisfactory reconstruction. We will see a numerical confirmation of this assumption in the next section.

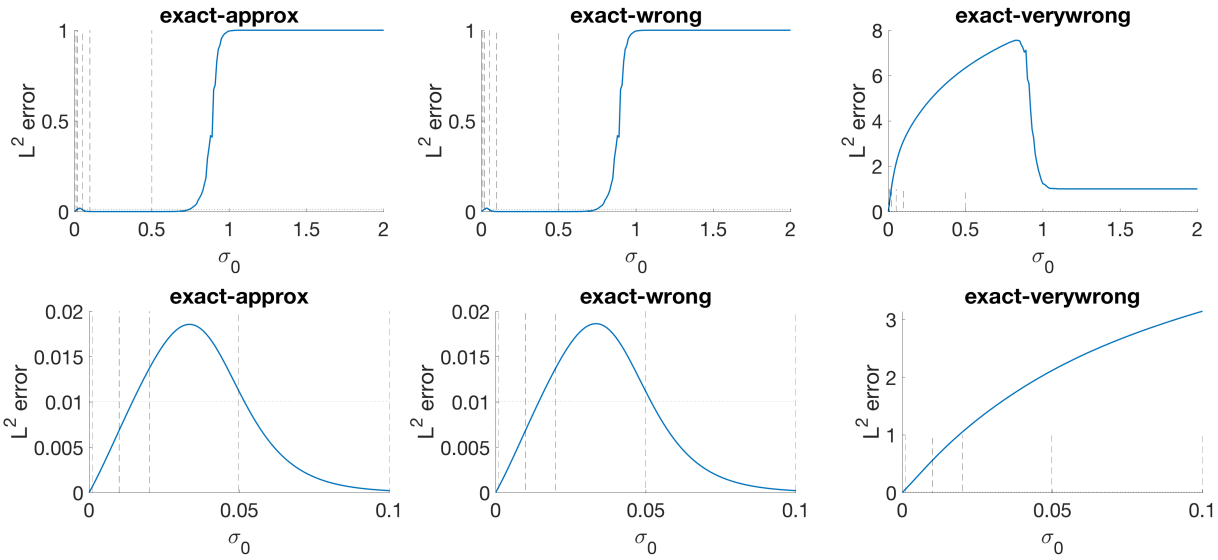

Figure 12: 1D analog for the 2D example of dissipative TRAC – Relative L^2-error between the approximations of the TRAC method and the exact dissipative TRAC, computed in $[x_{B^+}, x_R]$: 1^{st}-order approximated TRAC ('approx', left), 0^{th}-order approximated TRAC ('wrong', centre) and standard TRAC without dissipation ('very wrong', right). The dotted horizontal line shows the 1% threshold. The bottom row is a zoom-in of the top row for a narrower range of σ_0 to exhibit the special behaviour as σ_0 is small.

3.3 Numerical results – TRAC problem

Finally, we present the numerical results for the experiment described in Section 3.1. In the following, we are solving the problem to reconstruct the scattered wavefield

$$\begin{cases} -\omega^2\mu_0\mu_r\left(\omega\varepsilon_0\varepsilon_r + i\sigma_0\right)v_R^S - \Delta v_R^S &= 0, & \text{in } \Omega\backslash B, \\ v_R^S &= \overline{u^S}, & \text{on } \Gamma(=\partial\Omega), \\ \mathrm{TRAC}[v_R^S] &= 0, & \text{on } \partial B, \end{cases} \tag{24}$$

and we use three types of trial domains:

(i) a square with 0^{th}-order Engquist-Majda-like complex conjugated boundary condition

$$\mathrm{TRAC}_0[v_R^S] \;=\; \frac{\partial v_R^S}{\partial n} + i\overline{k_\sigma} v_R^S \;;$$

(ii) a circle with 1^{st}-order Bayliss-Turkel-like complex conjugated boundary condition

$$\mathrm{TRAC}_1[v_R^S] \;=\; \frac{\partial v_R^S}{\partial n} + i\overline{k_\sigma} v_R^S - \frac{v_R^S}{2r} \;;$$

(iii) a square with 2^{nd}-order Engquist-Majda-like complex conjugated boundary condition

$$\mathrm{TRAC}_2[v_R^S] \;=\; \frac{\partial v_R^S}{\partial n} + i\overline{k_\sigma} v_R^S - \frac{1}{2i\overline{k_\sigma}} \frac{\partial^2 v_R^S}{\partial \tau^2}.$$

We give a derivation of the absorbing boundary conditions in 2D in Appendix A.2.1.

We show the resulting reconstructions in Figure 13. In the case of a square trial domain, it occurs that the reconstruction was not satisfactory and we first wondered if the cause could be a bad treatment of the corners. This is indeed a concern, see [53] for a description of this treatment in the context of the *TRAC* method. However, when performing the reconstruction with a circular trial domain, the same image seems to appear. Moreover, further tests have been performed for smaller values of σ_0, which gave satisfactory reconstructions: about 13% still for $\sigma_0 = 0.01$ and trial domain (iii), for comparison the relative error for $\sigma_0 = 0$ was 11%. Thus, it looks like there is indeed an upper bound for σ_0 up to which the *TRAC* method may perform in a satisfactory way.

Consequently, we plot the relative L^2-error in Figure 14. We can observe two main things: First, for large values of σ_0 the curve seems to converge to 100%; Second, we can again exhibit a specific behaviour for smaller values of σ_0, with a local maximum occurring around $\sigma_0 = 0.02$ for trial domain types (i) and (ii), and $\sigma_0 = 0.034$ for trial domain type (iii). Those are very similar values to the calculated ones in the 1D analogy. However, although the curve is decreasing after this local maximum, the relative error remains large, suggesting a bad reconstruction.

To conclude, if we want to work with the dissipation of the soil as proposed in the experiment of Section 3.1, we may not be able to use the *TRAC* method with dissipation directly, but we need to find an alternative, perhaps with a smaller value of σ_0. This will be explored in further work.

As a more positive note, we would like to show a last example where $\sigma_0 = 0.01$, i.e., five times smaller than previously but still significant. We also choose a hexagonal shape for trial domain B to endorse the feasibility of the method for any shapes of B, with a 2^{nd}-order Engquist-Majda-like boundary condition. In Figure 15, we display the expected reconstruction versus the TRAC one and we observe very little discrepancy, which is confirmed by a relative L^2-error of 10.88%, the smallest error observed for this example when compared with the square (13.26% using (iii), 26.64% using (i)) and circular (21.12% using (ii)) trial domain B. Definitely, under a given value of the dissipation, reconstructions can be very accurate, i.e., error similar to the case without dissipation. Therefore it is useful to make this analysis to check the eligibility of the dissipative *TRAC* method depending on the dissipation present in the experiment.

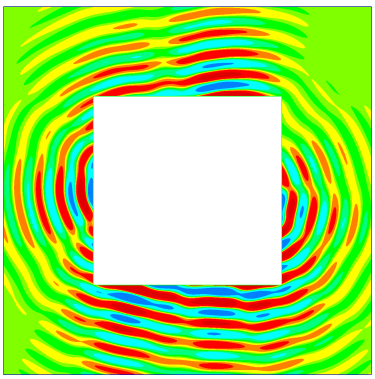

(a) Expected reconstruction for a square trial domain (real part)

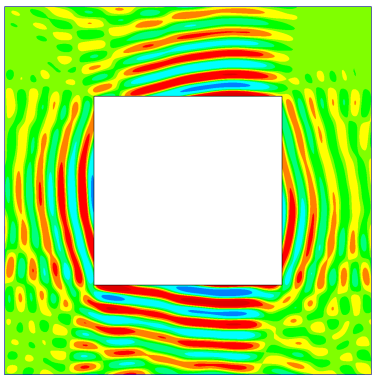

(b) Reconstruction with 0^{th} ABC (real part) – Error: 72.77%

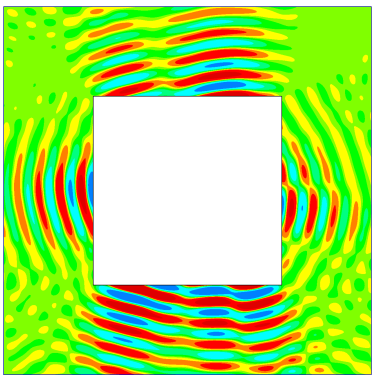

(c) Reconstruction with 2^{nd} ABC (real part) – Error: 46.99%

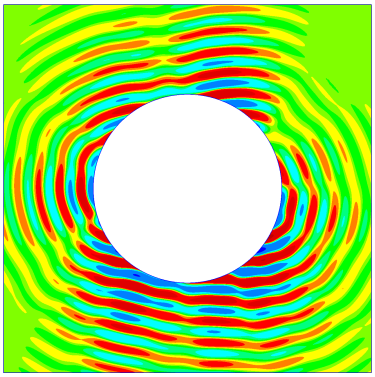

(d) Expected reconstruction for a circular trial domain (real part)

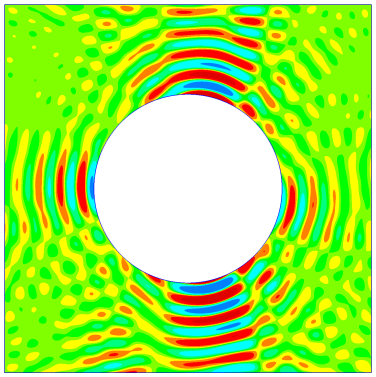

(e) Reconstruction with 1^{st} ABC (real part) – Error: 102.31%

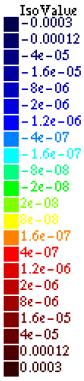

Figure 13: Numerical experiment in 2D – TRAC method with dissipation $\sigma_0 = \exp(-3)$. Results depending on the type of trial domain. The scale is the same for all the graphs.

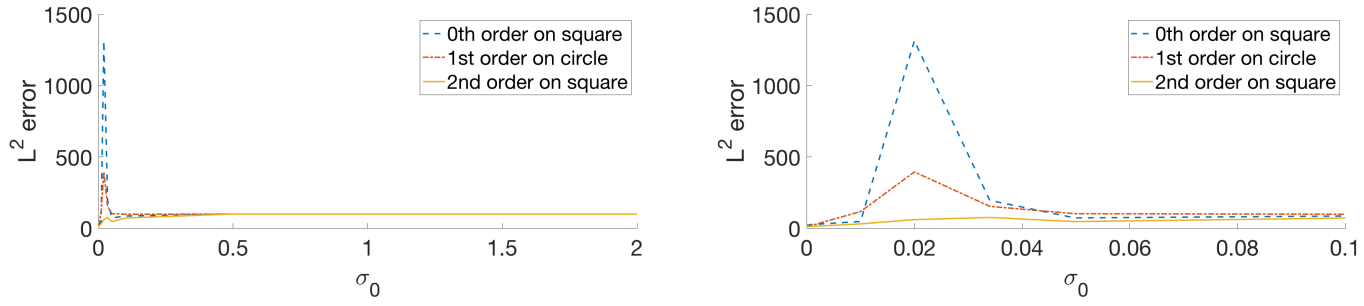

Figure 14: Numerical experiment in 2D – TRAC method with varying dissipation σ_0. Relative L^2-error for the three types of trial domains with respect to $\sigma 0 = [0, 0.0001, 0.001, 0.01, 0.02, 0.034, \exp(-3), 0.1, 0.5, 2]$ (left) and zoom-in (right).

4 Conclusion, discussion and perspective

In this paper, we explored the feasibility and the limit of the *TRAC* method in the presence of dissipation in the model. Dissipation indeed annihilates the time reversibility of the wave equation, and an anti-dissipative term is added in the time-reversed problem, which jeopardises the stability of the solution. We then conducted an analysis in one-space dimension and fre-

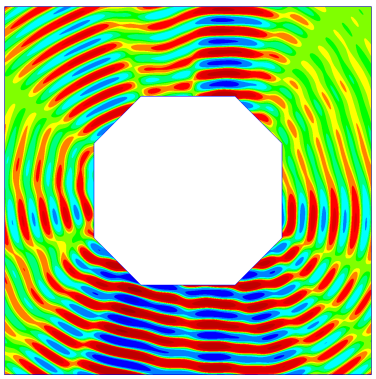

(a) Expected image for a hexagonal trial domain (real part)

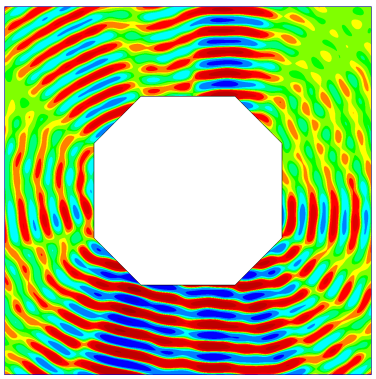

(b) Reconstruction with 2^{nd} ABC (real part) – Error: 10.88%

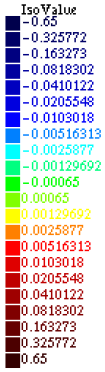

Figure 15: Numerical experiment in 2D – TRAC method with dissipation $\sigma_0 = 0.01$ with a hexagonal trial domain. The scale is the same for all the graphs.

quency domain to prove that the *TRAC* method using an exact absorbing boundary condition gives an exact reconstruction of the targeted wavefield. Furthermore, since the exact absorbing boundary condition in the frequency domain does not lead to a differential operator in the time domain after inverse Fourier Transform, we investigated three possible variants to the exact *TRAC* method with different levels of approximation. Ranges of values for the dissipation have been demonstrated for which the approximated *TRAC* methods can still give satisfactory reconstructions. We also see that there exists a given value of the dissipation from which the reconstruction will always be poor. Finally, we proposed a numerical example in the frequency domain and two-space dimension to check the feasibility of the *TRAC* method in presence of dissipation.

A part II studying heterogeneous media and a transition to the time domain is planned. As it stands, the current dissipative version of the *TRAC* method is not yet transposable to the time domain. Another level of approximation is needed to get a differential operator, nicer to implement, after inverse Fourier Transform. This additional approximation will be investigated in the frequency domain and two-space dimension for homogeneous dissipative media. A second question to be explored is about heterogeneous media. We will study the *TRAC* method when the heterogeneity of the ambient medium is known and, then, when only an average homogeneous approximation is used. Finally, we plan to extend our findings to the time domain in two-space dimensions.

5 Acknowledgments

MC would like to thank the University of Auckland for granting her a Summer Research Scholarship from December 2021 to February 2022, which allowed her to discover this branch of Applied Mathematics and contribute to this paper.

A Derivation of the ABC in presence of dissipation

A.1 In the frequency domain and one-space dimension (1D)

In this section, we propose to derive an artificial boundary condition for the Helmholtz equation that allows us to model infinite domains while performing numerical simulations in homogeneous,

but dissipative, media. We recall that the Helmholtz equation reads:

$$-\omega^2 \kappa u(x) - u''(x) \;=\; 0, \qquad \forall\, x \in \mathbb{R}, \tag{25}$$

where ω denotes the frequency and $\kappa \in \mathbb{C}$ represents the physical properties:

$$\kappa = \frac{1}{c^2}\left(1 - i\frac{\sigma}{\omega}\right),$$

Then, the general solution u can be written:

$$u(x) \;=\; C_1\, e^{\lambda_\sigma\, x} \;+\; C_2\, e^{-\lambda_\sigma\, x}, \tag{26}$$

for two constants to be determined, $C_1, C_2 \in \mathbb{C}$, and

$$\lambda_\sigma \;:=\; \sqrt{-\omega^2\kappa} \;=\; i\frac{\omega}{c}\sqrt{1 - i\frac{\sigma}{\omega}}. \tag{27}$$

We recall that all coefficients, c, ω are positive numbers and σ is nonnegative here. Hence,

$$\lambda_\sigma \;=\; \frac{\omega}{c}\left[\sqrt{\frac{1}{2}\left(\sqrt{1+\frac{\sigma^2}{\omega^2}} - 1\right)} + i\sqrt{\frac{1}{2}\left(\sqrt{1+\frac{\sigma^2}{\omega^2}} + 1\right)}\right].$$

Note that if $\sigma = 0$, λ_σ becomes the expected $i\omega/c$. From this form of λ_σ, we can deduce the following:

- $\mathrm{Re}(\lambda_\sigma) \geq 0$ for any positive values of c, ω and nonnegative values of σ
- $\mathrm{Im}(\lambda_\sigma) \geq \omega/c > 0$ for any positive values of c, ω and nonnegative values of σ
- the solution $e^{\lambda_\sigma\, x}$ is damped and vanishes when x goes to $-\infty$, but will increase exponentially as x goes to ∞
- the solution $e^{-\lambda_\sigma\, x}$ is damped and vanishes when x goes to ∞, but will increase exponentially as x goes to $-\infty$

As a result, we want to derive absorbing boundary conditions that will let pass the damped solution and cancel the exponentially increasing one.

Proposition A.1. *Assume that we want to solve* (25) *in the bounded domain* (x_L, x_R) *while modelling an infinite domain. Then the absorbing boundary condition for the dissipative Helmholtz equation in one-space dimension is exact and reads:*

$$\begin{cases} i\dfrac{\omega}{c}\sqrt{1 - i\dfrac{\sigma}{\omega}}\,u - u' = 0, & \text{on } \{x_L\}, \\[2ex] i\dfrac{\omega}{c}\sqrt{1 - i\dfrac{\sigma}{\omega}}\,u + u' = 0, & \text{on } \{x_R\}. \end{cases}$$

Proof. For the proof, we will use the notation λ_σ as defined in (27) for the sake of simplicity.

Let's start by considering the boundary condition on $\{x_L\}$ from waves propagating towards $-\infty$. As said above, the only dissipative solution is $e^{\lambda_\sigma\, x}$, while the other term will increase exponentially. By plugging the general solution (26) into the absorbing boundary condition, we get:

$$\begin{aligned} \lambda_\sigma u(x_L) - u'(x_L) &= \lambda_\sigma(C_1 e^{\lambda_\sigma\, x_L} + C_2 e^{-\lambda_\sigma\, x_L}) - (C_1\lambda_\sigma e^{\lambda_\sigma\, x_L} + C_2(-\lambda_\sigma)e^{-\lambda_\sigma\, x_L}) \\ &= 2\lambda_\sigma C_2 e^{-\lambda_\sigma\, x_L} \\ &= 0, \end{aligned}$$

which can be only achieved if $C_2 = 0$, i.e., only the dissipative wavefield $e^{\lambda_\sigma x}$ propagates through $\{x_L\}$.

The same calculation can be done on $\{x_R\}$ to show that C_1 must vanish to keep only the dissipative solution $e^{-\lambda_\sigma x}$ as x goes to $+\infty$. □

A.2 In the frequency domain and two-space dimension (2D)

Let's first remind three well-known absorbing boundary conditions in 2D without dissipation:

1. First order Engquist-Majda boundary condition [19] on linear boundaries (also zero-th order Bayliss-Turkel boundary condition [20] on circular boundaries):

$$i\omega u + c\frac{\partial u}{\partial n} = 0,$$

   where $\partial/\partial n$ denotes the external normal derivative;

2. First order Bayliss-Turkel boundary condition [20] on circular boundaries:

$$i\omega u + c\frac{\partial u}{\partial n} + \frac{cu}{2r} = 0,$$

   where $\partial/\partial n$ denotes the external normal derivative and r is the radius of the circular boundary;

3. Second order Engquist-Majda boundary condition [19] on linear boundaries:

$$-\omega^2 cu + i\omega\frac{\partial u}{\partial n} + \frac{c^2}{2}\frac{\partial^2 u}{\partial \tau^2} = 0,$$

   where $\partial/\partial n$ denotes the external normal derivative and $\partial^2/\partial\tau^2$ the second tangential derivative.

A.2.1 Derivation for a planar boundary

For the purpose of this paper, we derive analog absorbing boundary conditions including the dissipation term. We proceed as in [63] for planar boundaries, since our goal is to work with second order boundary conditions on square computational domains. The dissipative Helmholtz equation reads:

$$-\omega^2\kappa u(x,y) - \frac{\partial^2 u}{\partial x^2}(x,y) - \frac{\partial^2 u}{\partial y^2}(x,y) \;=\; 0, \quad \forall\,(x,y)\in\mathbb{R}^2, \tag{28}$$

the dissipation coefficient being in $\kappa \in \mathbb{C}$ as in (2) (or in Remark 1.1). To derive the boundary condition, we first consider the solution u to (28) in the right half space $x \geq 0$ independently of the boundary condition satisfied at $x = 0$, as a first example. The other half-planes can be derived similarly.

We take the Fourier transform in $y \in \mathbb{R}$, using η as dual variable:

$$-\omega^2\kappa\hat{u}(x) - \frac{\partial^2 \hat{u}}{\partial x^2}(x) + \eta^2\hat{u}(x) \;=\; 0, \quad \forall\, x \geq 0. \tag{29}$$

The solution to (29) takes the form:

$$\hat{u}(x) \;=\; A_- e^{\lambda_\sigma^- x} + A_+ e^{\lambda_\sigma^+ x}, \quad \forall\, x \geq 0. \tag{30}$$

Since $\lambda_\sigma^\pm := \pm\sqrt{\eta^2 - \omega^2\kappa}$ is a complex value, we need to check the sign of the real part and the imaginary part, to consider only the solution with a vanishing evanescent component, i.e., a negative real part. To write down the square root of $\lambda_\sigma^\pm$, we use the following notation for $\kappa := \alpha - i\beta, \quad \alpha, \beta \geq 0$, and we get:

$$\lambda_\sigma^- = -\sqrt{\frac{(\eta^2 - \omega^2\alpha) + \sqrt{(\eta^2 - \omega^2\alpha)^2 + (\omega^2\beta)^2}}{2}} - i\sqrt{\frac{-(\eta^2 - \omega^2\alpha) + \sqrt{(\eta^2 - \omega^2\alpha)^2 + (\omega^2\beta)^2}}{2}},$$

$$\lambda_\sigma^+ = \sqrt{\frac{(\eta^2 - \omega^2\alpha) + \sqrt{(\eta^2 - \omega^2\alpha)^2 + (\omega^2\beta)^2}}{2}} + i\sqrt{\frac{-(\eta^2 - \omega^2\alpha) + \sqrt{(\eta^2 - \omega^2\alpha)^2 + (\omega^2\beta)^2}}{2}}.$$

By analysing the signs, we see that

- If $\eta^2 \geq \omega^2\alpha$, then $\mathrm{Re}(\lambda_\sigma^+) \geq (\eta^2 - \omega^2\alpha) \geq 0$ and $\mathrm{Im}(\lambda^+) \geq 0$.
- If $\eta^2 \leq \omega^2\alpha$, then $\mathrm{Re}(\lambda_\sigma^+) \geq 0$ and $\mathrm{Im}(\lambda^+) \geq |\eta^2 - \omega^2\alpha| \geq 0$.
- Symmetrical results can be obtained for λ_σ^-, namely, $\mathrm{Re}(\lambda_\sigma^-) \leq 0$ and $\mathrm{Im}(\lambda_\sigma^-) \leq 0$.

As a result, since we only consider the solution propagating towards the infinity, coefficient A_+ must vanish, and the exact absorbing boundary condition for $\hat{u}(x) = A_- e^{\lambda_\sigma^- x}$ read:

$$\frac{\partial \hat{u}}{\partial x} - \lambda_\sigma^- \hat{u} = 0, \qquad \text{at } x = 0, \tag{31}$$

with

$$\lambda_\sigma^- = -\sqrt{\eta^2 - \omega^2\kappa} = -i\omega\sqrt{\kappa}\sqrt{1 - \frac{\eta^2}{\omega^2\kappa}}. \tag{32}$$

We need to take the inverse Fourier Transform to go back to the y-coordinate. In the current form, the inverse Fourier transform of (31) will not be a differential equation, and thus, will not be costly to implement. We propose to approximate it by a Taylor expansion. Let's assume that $|\eta^2/(\omega^2\kappa)|$ is small enough[5], then the $0th$-order approximation of (31) becomes:

$$\frac{\partial \hat{u}}{\partial x} + i\omega\sqrt{\kappa}\hat{u} = 0, \qquad \text{at } x = 0,$$

which translates, after inverse Fourier Transform, into:

$$\frac{\partial u}{\partial x} + i\omega\sqrt{\kappa}u = 0, \qquad \text{at } x = 0, \forall\, y \in \mathbb{R}.$$

A second order approximation is also conceivable and yields:

$$\frac{\partial \hat{u}}{\partial x} + i\omega\sqrt{\kappa}\left(1 - \frac{\eta^2}{2\omega^2\kappa}\right)\hat{u} = 0, \qquad \text{at } x = 0,$$

which translates, after inverse Fourier Transform, into:

$$\frac{\partial u}{\partial x} + i\omega\sqrt{\kappa}u - \frac{1}{2i\omega\sqrt{\kappa}}\frac{\partial^2 u}{\partial y^2} = 0, \qquad \text{at } x = 0, \forall\, y \in \mathbb{R}.$$

Similar derivation can be done for the other three half-planes and we obtained the following absorbing conditions for straight boundaries, where n and τ denote respectively the normal and the tangential coordinates:

[5]small values of $|\eta^2/(\omega^2\kappa)|$ correspond to waves whose propagation direction is close to the normal to the artificial boundary, see [63]

– $0th$-order:

$$\frac{\partial u}{\partial n} + i\omega\sqrt{\kappa}u \;=\; 0. \tag{33}$$

– $2nd$-order:

$$\frac{\partial u}{\partial n} + i\omega\sqrt{\kappa}u - \frac{1}{2i\omega\sqrt{\kappa}}\frac{\partial^2 u}{\partial \tau^2} \;=\; 0. \tag{34}$$

Remark A.1. Note that these absorbing boundary conditions are easily implemented in the frequency domain. However, the inverse Fourier Transform in time will again not lead to a partial differential equation and may be too costly to implement. This is the main motivation of this study. In the current form, $\sqrt{\kappa}$ prevents a direct translation, though. Approximations will need investigations, which we aim to study in a Part II. ■

A.2.2 Numerical results

To conclude this section, we propose to show some numerical examples that validate the absorbing boundary conditions (33) and (34). The numerical experiments will be performed using the software FreeFem++ [62].

For this experiment, we choose a frequency ν equal to 1 GHz, and $\omega = 2\pi\nu$ denotes the angular frequency in the Helmholtz equation. The medium is assumed to be homogeneous and dissipative, and its physical characteristics are described using electromagnetic notations:

$$\kappa \;:=\; \mu_0\left(\varepsilon_0 - i\sigma/\omega\right),$$

where μ_0 and ε_0 denote the magnetic permeability and the electric permittivity in the vacuum, respectively. Electric conductivity σ will be varying for the purpose of the numerical experiment. We also introduce the wavelength, λ, computed from the speed of light c_0 in the vacuum and the frequency:

$$\lambda \;:=\; \frac{c_0}{\nu} = \frac{1}{\nu\sqrt{\mu_0\varepsilon_0}}.$$

We choose a squared domain with a point source at the centre:

$$f(x,y) \;:=\; e^{-\frac{x^2+y^2}{\delta^2}},$$

with $\delta = 10^{-3}$. At the boundary, we use either the 0^{th}-order or the 2^{nd}-order absorbing boundary condition (33)-(34). For the discretisation, we use $\mathbb{P}^2$-Finite Elements.

• *Experiment 1 – Illustration*

In Figure 16, we display the real part of the solution to the dissipative Helmholtz equation. We actually only show the north-east corner, and the rest can be deduced by symmetry. We performed four tests using the dissipation $\sigma = 0.05$: (a) using (33) on a squared domain of length 20λ, i.e., distance to the source of 10λ, (b) using (34) with a distance to the source of 10λ, (c) using (33) with a distance to the source of 20λ (length of squared domain of 40λ), and (d) using (34) with a distance to the source of 20λ.
As expected, the solution is decaying faster than the non-dissipative counterpart (tests performed but not displayed) and we also notice that the ABC becomes more accurate as the boundary is farther from the source term. This is especially visible at the corners.

• *Experiment 2 – Quantification of the error*

Let's take the solution performed with the 2^{nd}-order absorbing boundary condition, $\mathbb{P}^2$-Finite Elements, on a squared mesh of edge 40λ (distance to the source of 20λ) as our reference solution

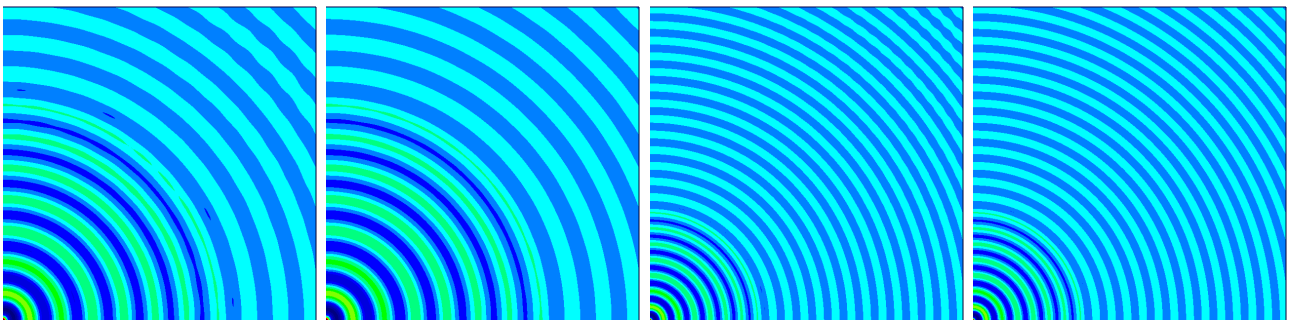

(a) Order 0 ABC, source at 10λ (b) Order 2 ABC, source at 10λ (c) Order 0 ABC, source at 20λ (d) Order 2 ABC, source at 20λ

Figure 16: ABC in 2D – Experiment 1. Zoom in the corner $x \geq 0$ and $y \geq 0$ of the damped solution to the dissipative Helmholtz equation with the boundary located at 10λ or 20λ from the point source. Dissipation $\sigma_0 = 0.005$.

to evaluate the error due to the approximated absorbing boundary condition.
To compute the error, we consider the solution recorded on a vertical line well inside the computational domain $x \in [-5\lambda, 5\lambda]$, at some distance from the point source. We perform the following three tests for $\sigma = 0$ (no dissipation for reference), $\sigma = 0.05$ and $\sigma = 0.2$:

- the recordings are at $5^{\frac{2}{3}}\lambda$ from the source in a computational domain of half-length $6^{\frac{2}{3}}\lambda$;
- the recordings are at $5^{\frac{2}{3}}\lambda$ from the source in a computational domain of half-length 10λ;
- the recordings are at 8λ from the source in a computational domain of half-length 10λ;

The relative L^2-error is reported in Table 2 and we can clearly see that the absorbing boundary condition is improved as the boundary is farther from the source. We also observe that the errors are of similar range of values as in the non-dissipative case with a better performance from the 2^{nd}-order ABC than the 0^{th}-order ABC, which indicates that the absorbing boundary condition is doing the right job.
We finally display the recordings (real part, imaginary part and modulus) in Figure 17. Again, the 2^{nd}-order ABC performs better than the 0^{th}-order ABC (less oscillatory), and the ABCs are more accurate on larger computational domains.

	Order 0 ABC (33)			Order 2 ABC (34)		
Dissipation|Distance	$5^{\frac{2}{3}}\lambda - 6^{\frac{2}{3}}\lambda$	$5^{\frac{2}{3}}\lambda - 10\lambda$	$8\lambda - 10\lambda$	$5^{\frac{2}{3}}\lambda - 6^{\frac{2}{3}}\lambda$	$5^{\frac{2}{3}}\lambda - 10\lambda$	$8\lambda - 10\lambda$
None ($\sigma = 0$)	18.62%	4.53%	5.37%	16.87%	2.91%	2.96%
$\sigma = 0.005$	18.11%	2.85%	3.41%	16.61%	2.24%	2.25%
$\sigma = 0.02$	17.48%	1.97%	2.14%	16.50%	1.92%	1.91%

Table 2: ABC in 2D – Experiment 2. Relative L^2-error computed at the receivers' location. Comparison between $0th$- and $2nd$-order absorbing boundary conditions for different values of dissipation σ.

Remark A.2. One could try to derive higher order absorbing boundary conditions, for different shapes of the boundary, or even for a specific model. For instance, we can also give the dissipative equivalent to the 1^{st}-order Bayliss-Turkel absorbing boundary condition, which recalls Equations (Atmo RBC HF 0) and (Atmo RBC HF 1) in [64] designed for 3D,

$$\frac{\partial u}{\partial n} + i\omega\sqrt{\kappa}u + \frac{u}{2r} \;=\; 0, \qquad r \text{ being the radius.} \tag{35}$$

For our purpose, only (33), (34) and (35) are actually used.

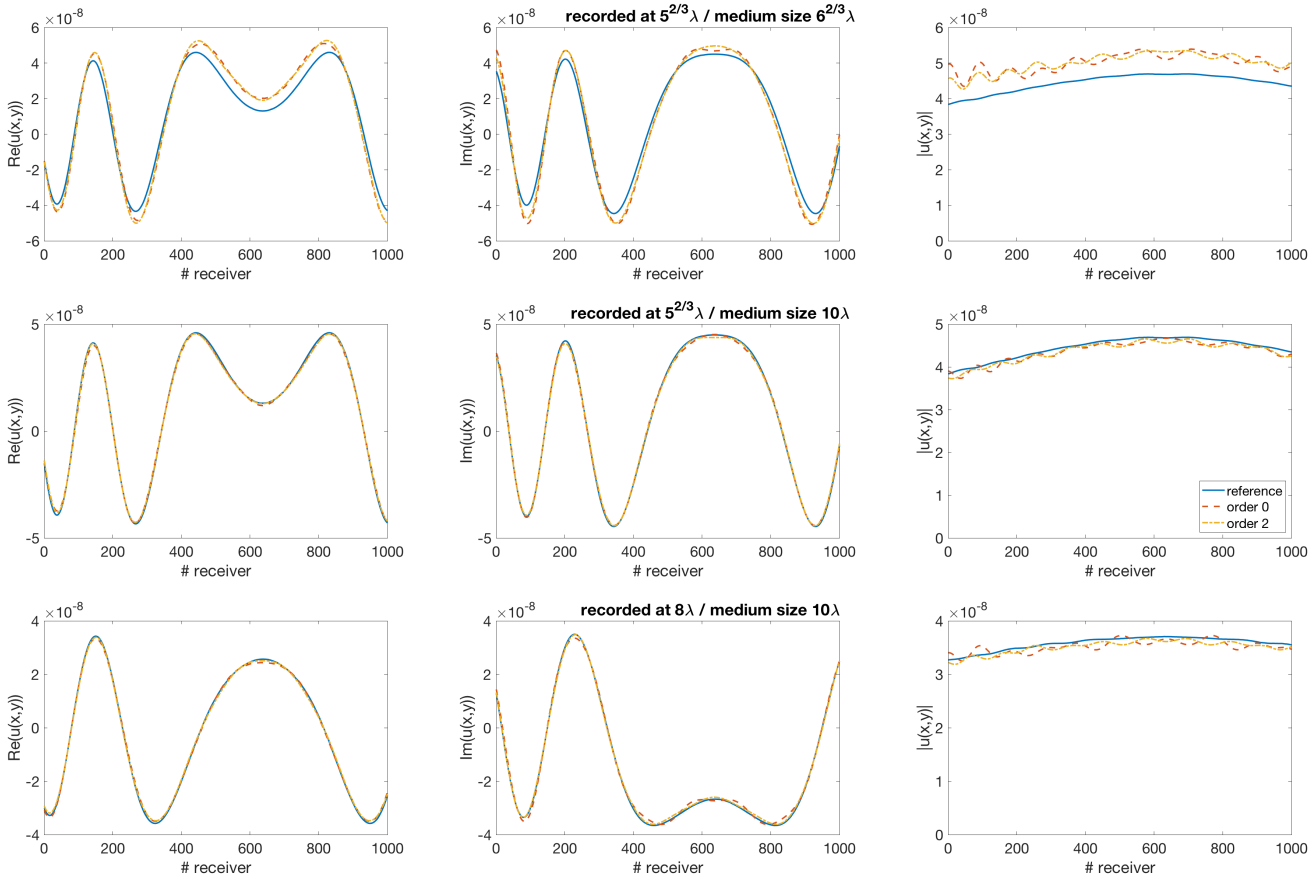

Figure 17: ABC in 2D – Experiment 2. Plots of the solution at the recording location (left: real part, centre: imaginary part, right: modulus) for the three tests and dissipation $\sigma = 0.05$

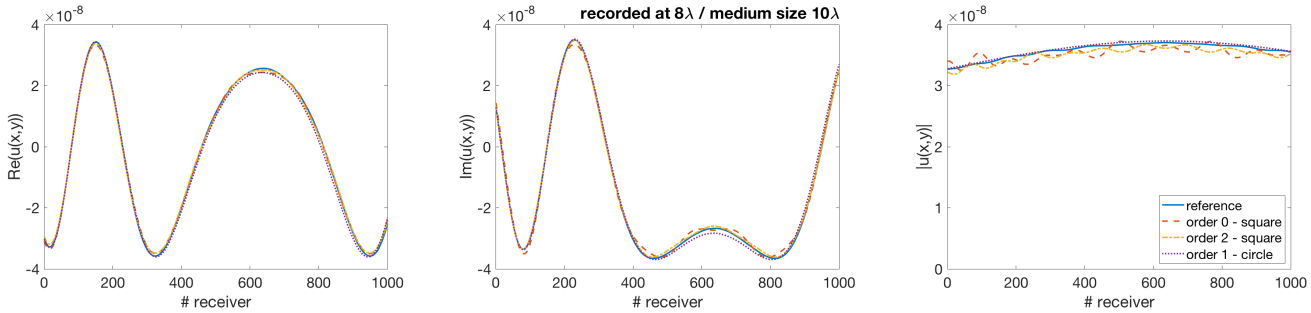

Figure 18: ABC in 2D – Experiment 2. Plots of the solution at the recording location (left: real part, centre: imaginary part, right: modulus) for the four tests and dissipation $\sigma = 0.05$

In Figure 18, we take the same settings and compare the results of Figure 17 with the solution obtained thanks to the dissipative 1^{st}-order Bayliss-Turkel absorbing boundary condition (35). The solution looks smoother (less oscillatory) and the amplitude is closer to the reference. This confirms that (35) may be a good update in the case of dissipation. ■

B Calculations in the frequency domain and one-space dimension (1D)

In this appendix, we compute all the solutions to the forward problems (4) and (6) and to the time reversed problems from Sections 2.2-2.4. Since we assume that the physical characteristics of the medium and the inclusion are piecewise constant functions, we can write the general solution as:

$$u(x) \;=\; C_1\, e^{ik_\sigma\, x} \;+\; C_2\, e^{-ik_\sigma\, x}, \tag{36}$$

where

$$k_\sigma = \frac{\omega_\sigma}{c} \qquad \text{and} \qquad \omega_\sigma = \omega\sqrt{1 - i\frac{\sigma}{\omega}}.$$

Constants C_1 and C_2 are then to be determined thanks to the provided boundary conditions specific to each problem.

Remark B.1. The derivation and computation of solutions is possible by hand for homogeneous media, e.g., we performed them with Maple. However, the general results could be extended to non-homogeneous media, since they do not rely on the homogeneity of the medium. We will not perform all the calculations, though. ■

B.1 Solutions to the forward cases

We assume that the computational domain is (x_L, x_R) and that an inclusion D is strictly enclosed in it, i.e., $[x_{D^-}, x_{D^+}] \subsetneq (x_L, x_R)$. We also assume that the source f is located at the extremity x_R.

Let's start with the incident wavefield, i.e., there is no inclusion in the computational domain yet.

Proposition B.1. *The incident wavefield u^I satisfies the problem*

$$\begin{cases} -\omega^2 u^I + i\omega\sigma_0 u^I - c_0^2 u^{I\prime\prime} &= 0, & \text{in } (x_L, x_R), \\ i\omega_{\sigma_0} u^I - c_0 u^{I\prime} &= 0, & \text{on } \{x_L\}, \\ i\omega_{\sigma_0} u^I + c_0 u^{I\prime} &= f, & \text{on } \{x_R\} \end{cases}$$

and is given by

$$u^I(x) = \frac{f}{2i\omega_{\sigma_0}} e^{ik_{\sigma_0}(x - x_R)}, \qquad \forall\, x \in [x_L, x_R].$$

Proof. The dissipative Helmholtz equation in 1D here is a constant coefficients second order ordinary differential equation with general solution

$$u^I(x) = Ae^{-ik_{\sigma_0}x} + Be^{ik_{\sigma_0}x},$$

where A and B are two complex coefficients to determine from the boundary conditions. We start by considering the absorbing boundary condition on $\{x_L\}$:

$$\begin{aligned} i\omega_{\sigma_0} u^I - c_0 u^{I\prime} &= i\omega_{\sigma_0}(Ae^{-ik_{\sigma_0}x} + Be^{ik_{\sigma_0}x}) - c_0(-ik_{\sigma_0}Ae^{-ik_{\sigma_0}x} + ik_{\sigma_0}Be^{ik_{\sigma_0}x}) \\ &= 2i\omega_{\sigma_0}Ae^{-ik_{\sigma_0}x} = 0 \qquad\qquad \Longrightarrow A = 0. \end{aligned}$$

Now, B can be deduce from the absorbing boundary condition on $\{x_R\}$:

$$\begin{aligned} i\omega_{\sigma_0} u^I(x_R) + c_0 u^{I\prime}(x_R) &= i\omega_{\sigma_0} B e^{ik_{\sigma_0}(x_R)} + c_0(ik_{\sigma_0}) B e^{ik_{\sigma_0}(x_R)} \\ &= 2i\omega_{\sigma_0} B e^{ik_{\sigma_0}(x_R)} = f \qquad \Longrightarrow B = \frac{f}{2i\omega_{\sigma_0}} e^{-ik_{\sigma_0}(x_R)}. \end{aligned}$$

□

For the purpose of readability, let's also called scattered field the following:

$$u^S(x) = -\frac{f}{2i\omega_{\sigma_0}} e^{ik_{\sigma_0}(x+x_R-2x_{D^+})}, \qquad \forall\, x \in [x_{D^+}, x_R].$$

Proposition B.2. *Assume that inclusion D is sound-soft. Then, the total wavefield u^T_{soft} is solution to*

$$\begin{cases} -\omega^2 u^T_{soft} + i\omega\sigma_0 u^T_{soft} - c_0^2 u^T_{soft}{}'' &= 0, & \text{in } (x_L, x_{D^-}) \cup (x_{D^+}, x_R), \\ i\omega_{\sigma_0} u^T_{soft} - c_0 u^T_{soft}{}' &= 0, & \text{on } \{x_L\}, \\ u^T_{soft} &= 0, & \text{on } \{x_{D^-}\} \text{ and on } \{x_{D^+}\}, \\ i\omega_{\sigma_0} u^T_{soft} + c_0 u^T_{soft}{}' &= f, & \text{on } \{x_R\}, \end{cases}$$

and reads:

$$u^T_{soft} = \begin{cases} u^I(x) + u^S(x) = \dfrac{f}{2i\omega_{\sigma_0}} \left(e^{ik_{\sigma_0}(x-x_R)} - e^{-ik_{\sigma_0}(x+x_R-2x_{D^+})} \right), & \forall\, x \in [x_{D^+}, x_R], \\ 0 & \text{otherwise.} \end{cases}$$

Proof. As previously, the general solution reads

$$u^T_{soft}(x) = Ae^{-ik_{\sigma_0}x} + Be^{ik_{\sigma_0}x},$$

where A and B are two complex coefficients to determine from the boundary conditions. We start by considering the absorbing boundary condition on $\{x_R\}$, which actually yields the same coefficient B as for the incident wave. Now, we use the Dirichlet boundary condition on $\{x_{D^+}\}$ to determine A

$$\begin{aligned} u^T_{soft}(x_{D^+}) &= Ae^{-ik_{\sigma_0}x_{D^+}} + \frac{f}{2i\omega_{\sigma_0}} e^{ik_{\sigma_0}(x_{D^+}-x_R)}, \\ &= 0, \qquad \Longrightarrow A = \frac{f}{2i\omega_{\sigma_0}} e^{-ik_0(x_R-2x_{D^+})}. \end{aligned}$$

□

Remark B.2. The scattered field is actually solution to

$$\begin{cases} -\omega^2 u^S + i\omega\sigma_0 u^S - c_0^2 u^{S\prime\prime} &= 0, & \text{in } (x_L, x_{D^-}) \cup (x_{D^+}, x_R), \\ u^S &= -u^I, & \text{on } \{x_{D^+}\}, \\ i\omega_{\sigma_0} u^S + c_0 u^{S\prime} &= 0, & \text{on } \{x_R\}, \end{cases}$$

and is equal to 0 in (x_L, x_{D^-}), since no signal goes through the sound-soft inclusion. ■

Proposition B.3. *Assume now that inclusion D is sound-hard. Then, the total wavefield u^T_{hard} is solution to*

$$\left\{\begin{array}{rcll} -\omega^2 u^T_{hard} + i\omega\sigma_0 u^T_{hard} - c_0^2 {u^T_{hard}}'' &=& 0, & \text{in } (x_L, x_{D^-}) \cup (x_{D^+}, x_R), \\ i\omega_{\sigma_0} u^T_{hard} - c_0 {u^T_{hard}}' &=& 0, & \text{on } \{x_L\}, \\ {u^T_{hard}}' &=& 0, & \text{on } \{x_{D^-}\} \text{ and on } \{x_{D^+}\}, \\ i\omega_{\sigma_0} u^T_{hard} + c_0 {u^T_{hard}}' &=& f, & \text{on } \{x_R\}, \end{array}\right.$$

and its solution differs only by a sign from the sound-soft case (change from a Dirichlet to a Neumann boundary condition):

$$u^T_{hard} = \left\{\begin{array}{ll} u^I(x) - u^S(x) = \dfrac{f}{2i\omega_{\sigma_0}} \left(e^{ik_{\sigma_0}(x-x_R)} + e^{-ik_{\sigma_0}(x+x_R-2x_{D^+})}\right), & \forall\, x \in [x_{D^+}, x_R], \\ 0 & \text{otherwise.} \end{array}\right.$$

Proof. The proof is entirely similar to the proof in the case of a sound-soft inclusion. Note that no signal goes through the sound-hard inclusion either. □

Finally, in the case of penetrable inclusions, we assume that the physical characteristics are piecewise constant

$$c(x) = \left\{\begin{array}{ll} c_0, & \text{in } (x_L, x_{D^-}) \cup (x_{D^+}, x_R), \\ c_D, & \text{in } (x_{D^-}, x_{D^+}), \end{array}\right. \quad \text{and} \quad \sigma(x) = \left\{\begin{array}{ll} \sigma_0, & \text{in } (x_L, x_{D^-}) \cup (x_{D^+}, x_R), \\ \sigma_D, & \text{in } (x_{D^-}, x_{D^+}), \end{array}\right.$$

Proposition B.4. *For a penetrable inclusion, the forward problem can be expressed as*

$$\left\{\begin{array}{rcll} -\omega^2 u^T + i\omega\sigma(x) u^T - c(x)^2 u^{T\prime\prime} &=& 0, & \text{in } (x_L, x_R), \\ i\omega_{\sigma_0} u^T - c_0 u^{T\prime} &=& 0, & \text{on } \{x_L\}, \\ i\omega_{\sigma_0} u^T + c_0 u^{T\prime} &=& f, & \text{on } \{x_R\}. \end{array}\right.$$

The solution reads

$$u^T = \left\{\begin{array}{ll} G_L(x) u^I(x), & \forall\, x \in [x_L, x_{D^-}], \\ G_D \left((k_{\sigma_D} - k_{\sigma_0}) e^{-ik_{\sigma_D}(x - x_{D^+} + 2x_{D^-})} + (k_{\sigma_D} - k_{\sigma_0}) e^{ik_{\sigma_D}(x + x_{D^+})}\right) & \forall\, x \in [x_{D^-}, x_{D^+}], \\ u^I(x) + G_R u^S(x), & \forall\, x \in [x_{D^+}, x_R]. \end{array}\right.$$

with

$$\begin{aligned} G_L(x) &= 4k_{\sigma_D} k_{\sigma_0} e^{ik_{\sigma_D}(x_{D^+} + x_{D^-})} e^{ik_{\sigma_0}(x_{D^+} - x_{D^-})}/C, \\ G_D &= 2k_{\sigma_0} u^I(x_{D^+})/C, \\ G_R &= (k^2_{\sigma_D} - k^2_{\sigma_0})(e^{ik_{\sigma_D} x_{D^-}} - e^{ik_{\sigma_D} x_{D^+}})/C, \\ \text{and} \quad C &= (k_{\sigma_D} + k_{\sigma_0})^2 e^{2ik_{\sigma_D} x_{D^+}} - (k_{\sigma_D} - k_{\sigma_0})^2 e^{2ik_{\sigma_D} x_{D^-}}. \end{aligned}$$

Proof. The general solution can be decomposed into three formulae

$$u^T = \left\{\begin{array}{ll} A_L\, e^{ik_{\sigma_0} x} + B_L\, e^{-ik_{\sigma_0} x}, & \forall\, x \in [x_L, x_{D^-}], \\ A_D\, e^{ik_{\sigma_D} x} + B_D\, e^{-ik_{\sigma_D} x}, & \forall\, x \in [x_{D^-}, x_{D^+}], \\ A_R\, e^{ik_{\sigma_0} x} + B_R\, e^{-ik_{\sigma_0} x}, & \forall\, x \in [x_{D^+}, x_R], \end{array}\right.$$

but must be $\mathcal{C}^1(x - L, x_R)$. Using continuity conditions on u^T and its first derivative on $\{x_{D^-}\}$ and $\{x_{D^+}\}$, we can build a 4×4 system to obtain the coefficients. We used Maple for the calculations, which we will not detail here. □

B.2 Solutions to the classical time reversal

As in Section 2.2, perfect classical time reversal occurs if the entire medium, with the inclusion, is known. This is the case, for instance, when performing the physical experiment by sending the recorded time-reversed signal in the original medium. Note the change of sign transforming the dissipation term into an anti-dissipative component.

For the sound-soft and sound-hard cases, we only consider the perfect time reversal on (x_{D^+}, x_R), since it is clear that no signal goes through these types of inclusion, i.e., the wavefield is zero in (x_L, x_{D^-}). We also assume that the only measurement is located at $\{x_R\}$ and that we know the inclusion-type at $\{x_{D^+}\}$. As a result, the perfect time reversal problem is:

- for a sound-soft inclusion:

$$\begin{cases} -\omega^2\, v^T_{soft,R} - i\omega\sigma_0 v^T_{soft,R} - c_0^2 {v^T_{soft,R}}'' &= 0, & \text{in } (x_{D^+}, x_R), \\ v^T_{soft,R} &= 0, & \text{on } \{x_{D^+}\}, \\ v^T_{soft,R} &= \overline{u^T_{soft}}, & \text{on } \{x_R\}. \end{cases}$$

- for a sound-hard inclusion:

$$\begin{cases} -\omega^2\, v^T_{hard,R} - i\omega\sigma_0 v^T_{hard,R} - c_0 {v^T_{hard,R}}'' &= 0, & \text{in } (x_{D^+}, x_R), \\ {v^T_{hard,R}}' &= 0, & \text{on } \{x_{D^+}\}, \\ v^T_{hard,R} &= \overline{u^T_{hard}}, & \text{on } \{x_R\}. \end{cases}$$

In both cases, it can be easily computed by hand or using a symbolic computer[6] that

$$v^T_{soft,R}(x) = \overline{u^T_{soft}}(x) \quad \text{and} \quad v^T_{hard,R}(x) = \overline{u^T_{hard}}(x)$$

for all $x \in [x_{D^+}, x_R]$, and by extension for all $x \in [x_L, x_{D^-}] \cup [x_{D^+}, x_R]$.

The penetrable case is obviously more complicated as the parameters vary and we can consider various configurations of receivers. We propose two possible configurations:

- Two measurements are used, one at $\{x_L\}$ and the other at $\{x_R\}$:

$$\begin{cases} -\omega^2\, v^T_R - i\omega\sigma(x) v^T_R - c(x)^2 v^{T\prime\prime}_R &= 0, & \text{in } (x_L, x_R), \\ v^T_R &= \overline{u^T}, & \text{on } \{x_L\} \cup \{x_R\}. \end{cases}$$

- Only one measurement at $\{x_R\}$ is available, we impose an out-going absorbing boundary condition[7] at $\{x_L\}$:

$$\begin{cases} -\omega^2\, v^T_R - i\omega\sigma(x) v^T_R - c(x)^2 v^{T\prime\prime}_R &= 0, & \text{in } (x_L, x_R), \\ -i\overline{\omega_\sigma} v^T_R - c_0 v^{T\prime}_R &= 0, & \text{on } \{x_L\}, \\ v^T_R &= \overline{u^T}, & \text{on } \{x_R\}. \end{cases}$$

Here again, the classical time reversal reconstruction of the total wavefield coincides exactly with the complex conjugated of the associated forward wavefield. The calculations require to split

[6] e.g., we used Maple.

[7] time-reversed, aka. complex conjugated from the forward counterpart.

the general solution in three, as for the forward case, and to use the continuity conditions. The result has been checked with Maple.

To perform numerical time reversal, it happens that the entire medium may not be known, e.g., we do not have information about the inclusion, only about the surrounding medium. The computation is then performed on (x_L, x_R) for any type of inclusions. As a result, classical time reversal consists in solving the time-reversed problem assuming that the medium is only composed with the surrounding characteristics, and we knowingly omit the presence of the inclusion. It is to be expected that the solution to this numerical time reversal will differ from the perfect time reversal, therefore, from the complex conjugate of the forward wavefield targeted. In Section 2.2, we propose two possible configurations, similar to the perfect time reversal for penetrable inclusions:

- two measurements are used, one at $\{x_L\}$ and the other at $\{x_R\}$;
- only one measurement at $\{x_R\}$ is available, we impose an out-going absorbing boundary condition[6] at $\{x_L\}$.

Proof. of **Proposition 2.3** Let's start with the case of two measurements. We recall the problem

$$\begin{cases} -\omega^2\, w_{R,2}^T \,-\, i\omega\sigma_0 w_{R,2}^T \,-\, c_0^2 {w_{R,2}^T}'' &=& 0, & \text{in } (x_L, x_R), \\ w_{R,2}^T &=& \overline{u^T}, & \text{on } \{x_L\} \cup \{x_R\}. \end{cases}$$

Then, the general solution is again

$$w_{R,2}^T(x) = Ae^{-i\overline{k_{\sigma_0}}x} + Be^{i\overline{k_{\sigma_0}}x}.$$

From the Dirichlet boundary conditions, we obtain the 2×2 system to solve

$$\begin{pmatrix} e^{-i\overline{k_{\sigma_0}}x_L} & e^{i\overline{k_{\sigma_0}}x_L} \\ e^{-i\overline{k_{\sigma_0}}x_R} & e^{i\overline{k_{\sigma_0}}x_R} \end{pmatrix} \begin{pmatrix} A \\ B \end{pmatrix} = \begin{pmatrix} \overline{u^T}(x_L) \\ \overline{u^T}(x_R) \end{pmatrix}.$$

and we get the solution

$$w_{R,2}^T(x) = \frac{\overline{u^T}(x_R)\left(e^{-i\overline{k_{\sigma_0}}(x-x_L)} - e^{i\overline{k_{\sigma_0}}(x-x_L)}\right) + \overline{u^T}(x_L)\left(e^{i\overline{k_{\sigma_0}}(x-x_R)} - e^{-i\overline{k_{\sigma_0}}(x-x_R)}\right)}{e^{-i\overline{k_{\sigma_0}}(x_R-x_L)} - e^{i\overline{k_{\sigma_0}}(x_R-x_L)}}, \quad \forall\, x \in [x_L, x_R].$$

For the case of one measurement, we recall that

$$\begin{cases} -\omega^2\, w_{R,1}^T \,-\, i\omega\sigma_0 w_{R,1}^T \,-\, c_0^2 {w_{R,1}^T}'' &=& 0, & \text{in } (x_L, x_R), \\ -i\overline{\omega_\sigma} w_{R,1}^T - c_0 {w_{R,1}^T}' &=& 0, & \text{on } \{x_L\}, \\ w_{R,1}^T &=& \overline{u^T}, & \text{on } \{x_R\}, \end{cases}$$

The general solution is again

$$w_{R,1}^T(x) = Ae^{-i\overline{k_{\sigma_0}}x} + Be^{i\overline{k_{\sigma_0}}x}.$$

Thanks to the absorbing boundary condition on $\{x_L\}$, we already see that $B = 0$. Finally, using the Dirichlet boundary condition on $\{x_R\}$, we obtain the result

$$w_R^T(x) \;=\; \overline{u^T}(x_R)e^{-i\overline{k_{\sigma_0}}(x-x_R)}, \qquad \forall\, x \in [x_L, x_R].$$

Note that these solutions hold for any type of inclusions: reflective or penetrable. □

B.3 Solutions to the TRAC problems

We have already described the exact TRAC problem and three approximations in Sections 2.1 and 2.3, and exhibit the general solution for each problem in terms of the total wavefield and the incident wavefield. In this section, we give some detail of the derivation of the solutions and apply the general formulae to three specific inclusion types. Thereafter, we also compute the corresponding error formulae that are used for the illustrations in Section 2.

Proof. of **Propositions 2.1, 2.4, 2.5 and 2.6** combined.
For the sake of simplicity, we only propose the derivation for the part of the solution in $[x_{B^+}, x_R]$. The solution in $[x_L, x_{B^-}]$ results from the symmetrical handling of the derivation.

We first notice that the general solution of (7), (13) and (15) is of the form

$$Ae^{-i\overline{k_{\sigma_0}}x} + Be^{i\overline{k_{\sigma_0}}x}, \qquad A, B \in \mathbb{C},$$

while for (17) it is

$$A_0 e^{-ik_0 x} + B_0 e^{ik_0 x}, \qquad A_0, B_0 \in \mathbb{C} \text{ and } k_0 = \frac{\omega}{c_0} \in \mathbb{R}.$$

Second, we observe that the absorbing boundary conditions used in the exact TRAC problem (7) and the standard TRAC problem (17) are the exact complex conjugated absorbing boundary conditions associated to the physical equation. The derivation of their solution will then be analog. Similarly, we can make the same conclusion about the derivation of the solutions to (13) and (15).

Let's consider the solution to the exact TRAC (7). From the complex conjugated absorbing boundary conditions on $\{x_{B^+}\}$, we have

$$\begin{aligned}
-i\overline{\omega_{\sigma_0}}v^T(x_{B^+}) + c_0 v^{T'}(x_{B^+}) &= -i\overline{\omega_{\sigma_0}}\left(Ae^{-i\overline{k_{\sigma_0}}x_{B^+}} + Be^{i\overline{k_{\sigma_0}}x_{B^+}}\right) \\
&\quad + c_0\left(-i\overline{k_{\sigma_0}}Ae^{-i\overline{k_{\sigma_0}}x_{B^+}} + i\overline{k_{\sigma_0}}Be^{i\overline{k_{\sigma_0}}x_{B^+}}\right) \\
&= -2i\overline{\omega_{\sigma_0}}Ae^{-i\overline{k_{\sigma_0}}x_{B^+}} \\
&= \mathrm{TRAC}^+_{ex}[\overline{u^I}](x_{B^+}), \qquad \Longrightarrow A = \frac{\mathrm{TRAC}^+_{ex}[\overline{u^I}](x_{B^+})}{-2i\overline{\omega_{\sigma_0}}}e^{i\overline{k_{\sigma_0}}x_{B^+}}.
\end{aligned}$$

Now, from the measurement, i.e., the Dirichlet boundary condition on $\{x_R\}$, we get

$$\begin{aligned}
v^T(x_R) &= \frac{\mathrm{TRAC}^+_{ex}[\overline{u^I}](x_{B^+})}{-2i\overline{\omega_{\sigma_0}}}e^{-i\overline{k_{\sigma_0}}(x_R - x_{B^+})} + Be^{i\overline{k_{\sigma_0}}x_R} \\
&= \overline{u^T}(x_R), \qquad \Longrightarrow B = \overline{u^T}(x_R)e^{-i\overline{k_{\sigma_0}}x_R} + \frac{\mathrm{TRAC}^+_{ex}[\overline{u^I}](x_{B^+})}{2i\overline{\omega_{\sigma_0}}}e^{-i\overline{k_{\sigma_0}}(2x_R - x_{B^+})}.
\end{aligned}$$

For the solution to (17), just replace $\overline{\omega_{\sigma_0}}$ by ω (therefore $\overline{k_{\sigma_0}}$ by k_0) and TRAC^+_{ex} by TRAC^+_{0th}.

For the other two problems, the complex conjugated absorbing boundary conditions is not exact. As a result, we cannot deduce A and B independently as before, but a 2×2-system must be solved

$$\begin{pmatrix} \left(i(\overline{\omega_{\sigma_0}} - \omega) + \frac{\sigma_0}{2}\right)e^{-i\overline{k_{\sigma_0}}x_{B^+}} & \left(i(\overline{\omega_{\sigma_0}} + \omega) - \frac{\sigma_0}{2}\right)e^{i\overline{k_{\sigma_0}}x_{B^+}} \\ e^{-i\overline{k_{\sigma_0}}x_R} & e^{i\overline{k_{\sigma_0}}x_R} \end{pmatrix}\begin{pmatrix} A \\ B \end{pmatrix} = \begin{pmatrix} \mathrm{TRAC}^+_{1st}[\overline{u^I}](x_{B^+}) \\ \overline{u^T}(x_R) \end{pmatrix}.$$

We obtain the result thanks to Maple. Finally, for the solution to (15) just replace $(i(\overline{\omega_{\sigma_0}} \mp \omega) \pm \sigma_0/2)$ by $i(\overline{\omega_{\sigma_0}} \mp \omega)$ and TRAC^+_{1st} by TRAC^+_{0th}. □

B.4 Simplification of the right-hand-side in the complex conjugated absorbing boundary conditions

We now describe explicitly the TRAC operators:

$$\begin{aligned}
\mathrm{TRAC}^{+}_{ex}[\overline{u^I}](x) &= -i\overline{\omega_{\sigma_0}}\,\overline{u^I}(x) + c_0\overline{u^I}'(x) \\
&= -i\overline{\omega_{\sigma_0}}\left(-\frac{f}{2i\overline{\omega_{\sigma_0}}}e^{-i\overline{k_{\sigma_0}}(x-x_R)}\right) + c_0\left(-\frac{f}{2i\overline{\omega_{\sigma_0}}}e^{-i\overline{k_{\sigma_0}}(x-x_R)}(-i\overline{k_{\sigma_0}})\right) \\
&= -2i\overline{\omega_{\sigma_0}}\left(-\frac{f}{2i\overline{\omega_{\sigma_0}}}e^{-i\overline{k_{\sigma_0}}(x-x_R)}\right) \\
&= fe^{-i\overline{k_{\sigma_0}}(x-x_R)} \quad \left(= -2i\overline{\omega_{\sigma_0}}\,\overline{u^I}(x)\right)
\end{aligned}$$

and

$$\begin{aligned}
\mathrm{TRAC}^{-}_{ex}[\overline{u^I}](x) &= -i\overline{\omega_{\sigma_0}}\,\overline{u^I}(x) - c_0\overline{u^I}'(x) \\
&= -i\overline{\omega_{\sigma_0}}\left(-\frac{f}{2i\overline{\omega_{\sigma_0}}}e^{-i\overline{k_{\sigma_0}}(x-x_R)}\right) - c_0\left(-\frac{f}{2i\overline{\omega_{\sigma_0}}}e^{-i\overline{k_{\sigma_0}}(x-x_R)}(-i\overline{k_{\sigma_0}})\right) \\
&= 0.
\end{aligned}$$

Thus $\mathrm{TRAC}^{+}_{ex}[\overline{u^I}](x_{B^+}) = fe^{-i\overline{k_{\sigma_0}}(x_{B^+}-x_R)}$ and $\mathrm{TRAC}^{-}_{ex}[\overline{u^I}](x_{B^-}) = 0$.

For each approximation of the TRAC methods, we also have:

- 1^{st}-order approximation:

$$\begin{aligned}
\mathrm{TRAC}^{+}_{1st}[\overline{u^I}](x) &= \left(-i(\omega+\overline{\omega_{\sigma_0}}) + \frac{\sigma_0}{2}\right)\left(\frac{-f}{2i\overline{\omega_{\sigma_0}}}e^{-i\overline{k_{\sigma_0}}(x-x_R)}\right) \\
\mathrm{TRAC}^{-}_{1st}[\overline{u^I}](x) &= \left(-i(\omega-\overline{\omega_{\sigma_0}}) + \frac{\sigma_0}{2}\right)\left(\frac{-f}{2i\overline{\omega_{\sigma_0}}}e^{-i\overline{k_{\sigma_0}}(x-x_R)}\right)
\end{aligned}$$

- 0^{st}-order approximation:

$$\begin{aligned}
\mathrm{TRAC}^{+}_{0th}[\overline{u^I}](x) &= i(\omega+\overline{\omega_{\sigma_0}})\left(\frac{f}{2i\overline{\omega_{\sigma_0}}}e^{-i\overline{k_{\sigma_0}}(x-x_R)}\right) \\
\mathrm{TRAC}^{-}_{0th}[\overline{u^I}](x) &= i(\omega-\overline{\omega_{\sigma_0}})\left(\frac{f}{2i\overline{\omega_{\sigma_0}}}e^{-i\overline{k_{\sigma_0}}(x-x_R)}\right)
\end{aligned}$$

References

[1] Mathias Fink, François Wu, Didier Cassereau, and Raoul Mallart. Imaging through inhomogeneous media using time reversal mirrors. *Ultrasonic Imaging*, 13(2):199 – 199, 1991.

[2] Mathias Fink. Time-reversal mirrors. *J. Phys. D: Appl. Phys.*, 26(9):1333, 1993.

[3] Mathias Fink and Claire Prada. Acoustic time-reversal mirrors. *Inverse Problems*, 17(1):R1, 2001.

[4] Claude Bardos and Mathias Fink. Mathematical foundations of the time reversal mirror. *Asymptot. Anal.*, 29(2):157–182, 2002.

[5] Carene Larmat, Jean-Paul Montagner, Mathias Fink, Yann Capdeville, Arnaud Tourin, and Eric Clévédé. Time-reversal imaging of seismic sources and application to the great Sumatra earthquake. *Geophys. Res. Lett.*, 33, 2006.

[6] Julien de Rosny and Mathias Fink. Overcoming the diffraction limit in wave physics using a time-reversal mirror and a novel acoustic sink. *Phys. Rev. Lett.*, 89(12):124301, 2002.

[7] Geoffroy Lerosey, Julien de Rosny, Arnaud Tourin, and Mathias Fink. Focusing beyond the diffraction limit with far-field time reversal. *Science*, 315(5815):1120–1122, 2007.

[8] Claire Prada and Mathias Fink. Eigenmodes of the time reversal operator: a solution to selective focusing in multiple-target media. *Wave Motion*, 20(2):151–163, 1994.

[9] Claire Prada, Sébastien Manneville, Dimitri Spoliansky, and Mathias Fink. Decomposition of the Time Reversal Operator: Application to detection and selective focusing on two scatterers. *J. Acoust. Soc. Am.*, 99(4):2067–2076, 1996.

[10] Peter Blomgren, George Papanicolaou, and Hongkai Zhao. Super-resolution in time-reversal acoustics. *J. Acoust. Soc. Am.*, 111(1):230–248, 2002.

[11] Liliana Borcea, George Papanicolaou, Chrysoula Tsogka, and James Berryman. Imaging and time reversal in random media. *Inverse Problems*, 18(5):1247, 2002.

[12] Jean-Pierre Fouque, Josselin Garnier, George Papanicolaou, and Knut Sølna. *Wave propagation and time reversal in randomly layered media*, volume 56 of *Stochastic Modelling and Applied Probability*. Springer, New York, 2007.

[13] Habib Ammari, Josselin Garnier, Wenjia Jing, Hyeonbae Kang, Mikyoung Lim, Knut Sølna, and Han Wang. *Mathematical and Statistical Methods for Multistatic Imaging*. Lecture Notes in Mathematics Series. Springer, Cham, 2013.

[14] Jean-Pierre Fouque, Josselin Garnier, André Nachbin, and Knut Sølna. Imaging of a dissipative layer in a random medium using a time reversal method. In Harald Niederreiter and Denis Talay, editors, *Monte Carlo and Quasi-Monte Carlo Methods 2004*, pages 127–145, Berlin, Heidelberg, 2006. Springer Berlin Heidelberg.

[15] Josselin Garnier and André Nachbin. Eddy viscosity for time reversing waves in a dissipative environment. *Phys. Rev. Lett.*, 93(15):154501, 2004.

[16] Franck Assous, Marie Kray, Frédéric Nataf, and Eli Turkel. Time reversed absorbing conditions. *Comptes Rendus Mathematiques*, 348(19-20):1063–1067, 2010.

[17] Franck Assous, Marie Kray, Frédéric Nataf, and Eli Turkel. Time Reversed Absorbing Condition: Application to inverse problem. *Inverse Problems*, 27(6):065003, 2011.

[18] Franck Assous, Marie Kray, and Frédéric Nataf. Time Reversed Absorbing Condition in the Partial Aperture Case. *Wave Motion*, 49(7):617–63, 2012.

[19] Björn Engquist and Andrew J. Majda. Absorbing boundary conditions for the numerical simulation of waves. *Math. Comp.*, 31(139):629–651, 1977.

[20] Alvin Bayliss and Eli Turkel. Radiation boundary conditions for wave-like equations. *Comm. Pure Appl. Math.*, 33(6):707–725, 1980.

[21] Thomas Hagstrom and S. I. Hariharan. A formulation of asymptotic and exact boundary conditions using local operators. *Applied Numerical Mathematics*, 27:403–416, 1998.

[22] Alvin Bayliss, Max Gunzburger, and Eli Turkel. Boundary conditions for the numerical solution of elliptic equations in exterior regions. *SIAM J. Appl. Math.*, 42(2):430–451, 1982.

[23] Michael Medvinsky, Eli Turkel, and Ulrich Hetmaniuk. Local absorbing boundary conditions for elliptical shaped boundaries. *J. Comput. Phys.*, 227(18):8254–8267, 2008.

[24] Michael Medvinsky and Eli Turkel. On surface radiation conditions for an ellipse. *JCAM*, 234:1647–1655, 2009.

[25] Xavier Antoine, Hélène Barucq, and Abderrahmane Bendali. Bayliss-turkel like radiation conditions on surfaces of arbitrary shape. *J. Math. Anal. Appl.*, 229:184–211, 1999.

[26] Hélène Barucq, Rabia Djellouli, and Anne-Gaëlle Saint-Guirons. Performance assessment of a new class of local absorbing boundary conditions for elliptical- and prolate spheroidal-shaped boundaries. *Appl. Numer. Anal.*, 59:1467–1498, 2009.

[27] Thomas Hagstrom and Timothy Warburton. A new auxiliary variable formulation of high-order local radiation boundary conditions: corner compatibility conditions and extensions to first-order systems. *Wave Motion*, 39(4):327–338, 2004.

[28] Dan Givoli, Thomas Hagstrom, and Igor Patlashenko. Finite element formulation with high-order absorbing boundary conditions for time-dependent waves. *Comput. Methods Appl. Mech. Engrg.*, 195(29–32):3666–3690, 2006.

[29] Eliane Bécache, Dan Givoli, and Thomas Hagstrom. High-order absorbing boundary conditions for anisotropic and convective wave equations. *J. Comput. Phys.*, 229(4):1099–1129, 2010.

[30] Sebastian Acosta. High-order surface radiation conditions for time-harmonic waves in exterior domains. *Comput. Meth. Appl. Mech. Engrg.*, 322:296–310, 2017.

[31] Axel Modave, Christophe Geuzaine, and Xavier Antoine. Corner treatments for high-order local absorbing boundary conditions in high-frequency acoustic scattering. *J. Comput. Phys.*, 401:109029, 2020.

[32] Symeon Papadimitropoulos and Dan Givoli. The double absorbing boundary method for the helmholtz equation. *Applied Numerical Mathematics*, 168:182–200, 2021.

[33] Philippe Marchner, Xavier Antoine, Christophe Geuzaine, and Hadrien Bériot. Construction and Numerical Assessment of Local Absorbing Boundary Conditions for Heterogeneous Time-Harmonic Acoustic Problems. *SIAM Journal on Applied Mathematics*, 2022. hal-03196015.

[34] Marcus J. Grote and Christoph Kirsch. Nonreflecting boundary condition for time-dependent multiple scattering. *J. Comput. Phys.*, 221(1):41–67, 2007.

[35] Marcus J. Grote and Imbo Sim. Local nonreflecting boundary condition for time-dependent multiple scattering. *J. Comput. Phys.*, 230(8):3135–3154, 2011.

[36] Sebastian Acosta. On-surface radiation condition for multiple scattering of waves. *Comput. Meth. Appl. Mech. Engrg.*, 283:1296–1309, 2015.

[37] Sailing He and Vaughan H. Weston. Wave-splitting and absorbing boundary condition for Maxwell's equations on a curved surface. *Mathematics and Computers in Simulation*, 50(5-6):435–455, 1999.

[38] Marcus J. Grote and Joseph B. Keller. Nonreflecting boundary conditions for Maxwell's equations. *J. Comput. Phys.*, 139(2):327–342, 1998.

[39] Marcus J. Grote. Local nonreflecting boundary condition for Maxwell's equations. *Comput. Meth. Appl. Mech. Engrg.*, 195(29-32):3691–3708, 2006.

[40] Robert L. Higdon. Radiation boundary conditions for elastic wave propagation. *SIAM J. Numer. Anal.*, 27(4):831–869, 1990.

[41] Marcus J. Grote. Nonreflecting boundary conditions for elastodynamic scattering. *J. Comput. Phys.*, 161(1):331–353, 2000.

[42] Daniel Rabinovich, Dan Givoli, Jacobo Bielak, and Thomas Hagstrom. A finite element scheme with a high order absorbing boundary condition for elastodynamics. *Comput. Methods Appl. Mech. Engrg.*, 200(23-24):2048–2066, 2011.

[43] Lionel Boillot, Hélène Barucq, Julien Diaz, and Henri Calandra. Absorbing Boundary Conditions for 3D Elastic TTI Modeling, Application to Time-Based and Time-Harmonic Simulations. In *EAGE Saint Petersburg International Conference & Exhibition*, Saint Petersburg, Russia, April 2016.

[44] John R. Berryhill. Wave-equation datuming. *Geophysics*, 44(206):132944, 1979.

[45] John R. Berryhill. Wave-equation datuming before stack. *Geophysics*, 49(11):2064–2066, 1984.

[46] Maya de Buhan and Marie Kray. A new approach to solve the inverse scattering problem for waves: combining the TRAC and the Adaptive Inversion methods. *Inverse Problems*, 29(8):085009, 2013.

[47] Marie Graff, Marcus J. Grote, Frédéric Nataf, and Franck Assous. How to solve inverse scattering problems without knowing the source term: a three-step strategy. *Inverse Problems*, 35(10):104001, 2019.

[48] Franck Assous and Frédéric Nataf. Full-waveform redatuming via a TRAC approach: A first step towards target oriented inverse problem. *J. Comput. Phys.*, 440:110377, 2021.

[49] Franck Assous, Marie Kray, and Frédéric Nataf. Time reversal techniques for multitarget identification. In *2013 IEEE International Ultrasonics Symposium (IUS)*, pages 143–145, July 2013. 21 - 25 July 2013, Prague, Czech Republic.

[50] Eyal Amitt, Dan Givoli, and Eli Turkel. Time reversal for crack identification. *Computational Mechanics*, 54(2):443–459, 2014.

[51] Eyal Amitt, Dan Givoli, and Eli Turkel. Combined arrival-time imaging and time reversal for scatterer identification. *Comput. Methods Appl. Mech. Engrg.*, 313:279–302, 2017.

[52] Daniel Rabinovich, Eli Turkel, and Dan Givoli. An augmented time reversal method for source and scatterer identification. *J. Comput. Phys.*, 375:99–119, 2018.

[53] Tomer Levin, Eli Turkel, and Dan Givoli. Obstacle identification using the trac algorithm with a second-order abc. *Int. J. Numer. Methods Eng.*, 118(2):61–92, 2019.

[54] Hélène Barucq, Nathan Rouxelin, and Sébastien Tordeux. Prandtl-Glauert-Lorentz based Absorbing Boundary Conditions for the convected Helmholtz equation. hal-03288930, 2021.

[55] Jerald L. Bauck. A note on fourier transform conventions used in wave analyses. *EngrXiv.org*, July 2018.

[56] Raymond C. Rumpf. Simple implementation of arbitrarily shaped total-field/scattered-field regions in finite-difference frequency-domain. *JPIER B*, 36:221–248, 2012.

[57] Amir M. Alani, Francesco Soldovieri, Ilaria Catapano, Iraklis Giannakis, Gianluca Gennarelli, Livia Lantini, Giovanni Ludeno, and Fabio Tosti. The use of ground penetrating radar and microwave tomography for the detection of decay and cavities in tree trunks. *Remote Sensing*, 11(18):2073, 2019.

[58] Andrew C.M. Austin. Uncertainty quantification and parameter estimation in the finite-difference frequency-domain method using polynomial chaos. *JPIER M*, 101:117–126, 2021.

[59] Franck Assous, Marie Kray, Frédéric Nataf, and Eli Turkel. Time Reversed Absorbing Conditions (TRAC) in the time and frequency domains. ACM, 2012. 1st International ICST Workshop on New Computational Methods for Inverse Problems.

[60] Albert Tarantola. Theoretical background for the inversion of seismic waveforms including elasticity and attenuation. *Pure and Applied Geophysics*, 128:365–399, 1988.

[61] Jan Igel. The Small-Scale Variability of Electrical Soil Properties – Influence on GPR Measurements. 12^{th} *International Conference on Ground Penetrating Radar*, 2008. June 16-19, Birmingham, UK.

[62] Frédéric Hecht. New development in FreeFem++. *J. Numer. Math.*, 20(3-4):251–265, 2012.

[63] Frédéric Nataf. Absorbing boundary conditions and perfectly matched layers in wave propagation problems. *Direct and inverse problems in wave propagation and applications*, 14:219–231, 2013.

[64] Hélène Barucq, Juliette Chabassier, Marc Duruflé, Laurent Gizon, and Michael Leguèbe. Atmospheric Radiation Boundary Conditions for the Helmholtz Equation. *ESAIM M2AN*, 52(3), 2018.